On the Evolution of Isolated, Nonlinear Vortices

JAMES C. McWILLIAMS

National Center for Atmospheric Research,[1] Boulder, CO 80307

GLENN R. FLIERL

Massachusetts Institute of Technology, Cambridge, MA 02139

(Manuscript received 28 December 1978, in final form 8 May 1979)

ABSTRACT

The evolution of an isolated, axially symmetric vortex is calculated with a quasi-geostrophic, adiabatic, hydrostatic, β-plane, two vertical mode model. The circumstances of greatest interest are those of weak friction and large vortex amplitude (strong nonlinearity). Systematic studies are made of the consequences of varying the frictional coefficient, the vortex amplitude, the vortex radius (relative to the deformation radius), the degree of nonlinear coupling between the two vertical modes and the initial vertical structure of the vortex.

Results of note include the following. Within the approximation of a single vertical mode model (i.e., in the absence of modal coupling), a baroclinic vortex has an increased westward and a finite meridional propagation speed when its amplitude is greater than infinitesimal. Both of these speeds, however, are limited by the wave speeds (as determined from infinitesimal amplitude theory) of the weak dispersion field outside the vortex. The vortex amplitude decay rate, in the limit of strong nonlinearity, is governed by the frictional coefficient rather than dispersion. When vertical modal coupling is included, the vortex propagation and decay rate can be altered. Asymptotically in time, the vortex approaches a state of deep compensation (i.e., beneath a shallow thermocline, there is no flow in phase with the upper ocean vortex), with a propagation velocity less rapid in the westward direction and more rapid in the meridional direction (compared to a single mode vortex), and with a decay rate again controlled by the friction coefficient. At earlier times, however, more bizarre behavior can occur; for example, a vortex with initially pure baroclinic mode vertical structure can behave as an eastward-propagating vortical modon for a brief interval.

This study focuses on vortices whose baroclinic component is of only one sign (a positive temperature extremum in the thermocline); however, because of a symmetry of the model chosen (in particular due to its quasi-geostrophic assumption), these solutions can be simply reinterpreted to apply to vortices of both signs.

1. Introduction

Intense vortices, referred to as Gulf Stream rings, are frequently observed in the region of the North Atlantic Ocean south and east of the Gulf Stream (Parker, 1971). They are formed by the pinching off of large-amplitude southward meanders of the Gulf Stream (Fuglister and Worthington, 1951) and thus have a characteristic direction of circulation (counterclockwise or cyclonic) and characteristic temperature and pressure extrema (cold and low, respectively). Similar vortices are observed elsewhere [e.g., near the Kuroshio current in the North Pacific (Cheney and Richardson, 1977)]. Most commonly, rings have been identified from hydrographic measurements: they are known to be *isolated* (i.e., frequently no other temperature extrema of comparable magnitude are nearby), highly *baroclinic* (i.e., horizontal temperature gradients and, by geostrophy, vertical shears of horizontal velocity are large), and strongly *nonlinear* (i.e., a ratio of the Rossby numbers associated with nonlinear advection and linear wave propagation, $V_0/\beta l^2$, is large).[2] Other characteristics of rings, about which there remain significant uncertainties, are the following. Their lifetimes are long and their rates of decay are slow. Cheney and Richardson (1974) observed one ring for nearly two years before it was reabsorbed in the Gulf Stream. During the time the ring was in deep water, its tangential transport, between zero and 1000 m depth, decreased by less than 25% in 8 months. Rings are observed over a wide geographical area. They are most prevalent near the Gulf Stream,

[1] The National Center for Atmospheric Research is sponsored by the National Science Foundation.

[2] β is the northward gradient of the Coriolis parameter (1.7×10^{-11} m^{-1} s^{-1} at 40° latitude); V_0 is a typical particle speed for the Gulf Stream or a ring ($\sim$0.8 m s^{-1}); and l is a typical pressure e-folding radius of a ring ($\sim$60 km). Thus, $V_0/\beta l^2 \approx 13$, which is large.

0022-3670/79/061155-28$11.00

where their propagation velocities are typically 3 cm s^{-1} toward the southwest, which is also the direction of flow for mean thermocline circulation (Lai and Richardson, 1977). Recently, a ring was observed far from the Gulf Stream near 27°N, 70°W, where the mean circulation is weak, moving toward the northwest at a few centimeters per second (Taft and Baronov *et al.*, 1978). The current structure of rings is poorly known beneath the thermocline; however, from recent observations with neutrally buoyant floats (Cheney, 1977) and electromagnetic velocity profilers (Sanford *et al.*, 1978) it appears that the deep flow lies within the range from pure baroclinic mode (zero total tangential transport) to compensated structure (zero deep flow) to flow weakly in phase with the upper layers. This range of vertical structures is also probably that for the Gulf Stream.

In our opinion, the present data are too incomplete to warrant a detailed fitting or hindcasting comparison with theoretical models. What we shall present is instead an idealized study of vortex behavior under circumstances which are similar to those of observed rings. Particular emphasis will be placed on the influence of nonlinearity. The specific problem addressed is that of the unforced evolution of an initially axially symmetric Gaussian vortex in a horizontally unbounded, otherwise quiescent ocean (numerically approximated as periodic on a scale large compared to the vortex diameter) within the dynamical approximations of two vertical layers (or modes), constant β, quasi-geostrophy, and adiabatic thermal balances (though we include a weak lateral momentum diffusion at least partly to ensure numerical stability).[3] Related calculations have been reported by Bretherton and Karweit (1975), with a six-layer quasi-geostrophic model, and Mied (1978), with a two-layer primitive equation model. The initial baroclinic vortex amplitudes used by these authors are considerably weaker than those in our study. In addition, we examine a wider range of circumstances (size, strength, vertical structure, etc.) than has been considered in previous work and are able to obtain solutions for longer time intervals and with smaller side boundary influence (i.e., a better approximation to an unbounded domain).[4]

This theoretical study is usefully seen in the context of several simple but extreme models of vortex behavior. In a uniformly rotating environment ($\beta = 0$), without friction, any stationary, axially symmetric vortex is a steady, though not necessarily stable, solution to the model described above, for arbitrary vortex strength and vertical structure (when the vertical and horizontal variations are mathematically separable). With the addition of lateral friction, but with β still zero, such a vortex remains stationary although its radial profile changes and its amplitude decreases with time.[5] These changes occur without nonlinear influence, whatever the vortex strength, and without changes in the vertical structure. For variable Coriolis parameter, however, an axially symmetric, small-amplitude frictionless vortex will propagate due west as well as rapidly disperse and decrease in amplitude unless its radius is large compared to the radius of deformation appropriate to its vertical modal structure (see Flierl, 1977). Different modal structures can be superimposed.

None of these models are generally satisfactory for interpreting Gulf Stream ring behavior. Our attention in this study will be focused on the combined effects of $\beta \neq 0$, which is essential to vortex propagation, and nonlinearity, which we shall show significantly alters the rates of propagation, decay and dispersion, and allows for strong interactions between different vertical modes.

2. Mathematical formulation

We shall use a hydrostatic, quasi-geostrophic, Boussinesq, rigid-lid model with a two-mode vertical structure representation. Under these conditions, a two-mode model is physically equivalent to either a two-layer or two-level model. If p_1 and p_2 are the pressures in the two layers (or at two levels), then they can be represented as a linear combination of the first two dynamical modal pressures p_T and p_C (the barotropic and first baroclinic, respectively) by the formulas

$$\left.\begin{aligned} p_1 &= p_T + \delta^{-1/2} p_C \\ p_2 &= p_T - \delta^{1/2} p_C \end{aligned}\right\}, \tag{2.1}$$

where δ $(=H_1/H_2)$ is the ratio of the undisturbed layer depths. The normalization in (2.1) is that which is consistent with orthonormal modes, i.e.,

$$\frac{1}{H}\int_{-H}^{0} dz F_\alpha(z) F_\beta(z) = \frac{1}{H_1 + H_2}\sum_{i=1}^{2} H_i F_\alpha(z_i) F_\beta(z_i)$$
$$= \delta_{\alpha\beta}; \quad \alpha, \beta = \{T, C\}, \tag{2.2}$$

where the $F_\alpha(z)$ are the vertical structure functions which multiply the modal pressures $p_\alpha(x,y,t)$ and

[3] It is perhaps equally important to list those dynamical processes which we shall not address, yet which are probably important for at least some ring behavior. Among them are lateral boundary effects, mean current effects, interactions with other eddies or rings, topographic effects and initial axial asymmetries.

[4] More recently, Mied and Lindemann (1979) have reported a more extensive set of numerical calculations with their two-layer primitive equation model.

[5] The combination of ageostrophic and frictional effects can lead to radial-vertical circulations (e.g., Charney, 1973). Schmitz and Vastano (1975) studied this mechanism, in combination with density diffusion, in modeling the observed decay of the temperature anomaly associated with a ring.

the z_i are the mean depths of the two layers or levels. Refer to Flierl (1978) for a thorough discussion of this equivalence.

The model equations are made nondimensional by the following characteristic scales for the dependent and independent variables:

$$\left.\begin{array}{ll} x, y \sim l & p_T, p_c \sim V_0 f_0 l \\ z \sim H_2 & \psi, \chi \sim V_0 l \\ t \sim (\beta l)^{-1}, & \end{array}\right\}, \qquad (2.3)$$

where V_0 is a particle speed, l a pressure e-folding radius, f_0 a value of the Coriolis parameter at a central latitude ($y = y_0$), and β the meridional gradient of the Coriolis parameter. In (2.3), ψ and χ are velocity streamfunctions associated with the barotropic and baroclinic modes, respectively (*n.b.*, $\psi = p_T$ and $\chi = p_C$ nondimensionally). In terms of these streamfunctions the nondimensional, modal, potential vorticity equations are

$$[m - 1][\nabla^2\psi_t + \psi_x + QJ(\psi,\nabla^2\psi) + QJ(\chi,\nabla^2\chi) + K_*\nabla^6\psi] = 0, \qquad (2.4a)$$

$$(\nabla^2 - \gamma^2)\chi_t + \chi_x + \hat{Q}J(\chi,\nabla^2\chi) + Q[m - 1][J(\chi,\nabla^2\psi) + J(\psi,\nabla^2\chi - \gamma^2\chi)] + K_*\nabla^6\chi = 0 \qquad (2.4b)$$

[cf. Eq. (2.11) of Flierl (1978)]. The parameters which appear in Eqs. (2.4) are

$$\left.\begin{array}{ll} Q = V_0/\beta l^2, & \gamma = l/R \\ \hat{Q} = \dfrac{1 - \delta}{\sqrt{\delta}}\, Q, & K_* = \dfrac{K_{\text{dimensional}}}{\beta l^5} \end{array}\right\}, \qquad (2.5)$$

and m, the vertical mode number of the model. The latter is a mathematical artifice which allows us to examine (2.4b) alone as a model for a single vertical mode, including only the nonlinearity of its self-interaction. When $m = 1$, this implies an ad hoc elimination of nonlinear coupling between the two modes, whereas when $m = 2$, Eqs. (2.4) become the correct two-mode equations. In Eq. (2.5), R $\{=[g'H_1H_2/(H_1 + H_2)]^{1/2}f_0^{-1}\}$ is the first baroclinic or internal radius of deformation, and g' is the reduced gravitational constant (i.e., the product of $g = 9.8$ m s^{-2} and the relative density difference between the two layers). All definitions involving vertical structure have been given in terms of the two-layer approximation; for an interpretation in terms of continuous vertical structure, $\hat{Q}$ and R would be defined by integral properties of the fluid (Flierl, 1978). The quantity $K_{\text{dimensional}}$ in (2.5) is the coefficient of a scale-selective, biharmonic lateral friction or momentum diffusion which appears as the final term in each of Eqs. (2.4). This frictional form is another artifice, currently in common practice (e.g., Bretherton and Karweit, 1975; Holland, 1978), which assures computational stability while leaving the larger scales of motion reasonably undamped, by consuming the enstrophy (mean-square vorticity) which can accumulate on the smallest resolved scales due to nonlinear transfers between scales. It will be seen to play an additional physical role in regulating the rate of vortex decay in many of our solutions. This effect should be believed only qualitatively because a biharmonic operator is undoubtedly a crude representation of the frictional processes in the ocean.

When the solutions of Eqs. (2.4) are isolated ones (i.e., ψ and $\chi \to 0$ as $|x^2 + y^2| \to \infty$), then several integral moment equations can be derived which will be helpful in interpreting vortex evolution. In an infinite horizontal domain, the following relations hold:

$$\left.\begin{array}{l} \text{(i)}\quad [m - 1]\displaystyle\iint dxdy\ \psi = 0 \\ \text{(ii)}\quad \gamma^2\dfrac{\partial}{\partial t}\displaystyle\iint dxdy\ \chi = 0 \\ \text{(iii)}\quad \gamma^2\dfrac{\partial}{\partial t}\displaystyle\iint dxdy\ x\chi = -\iint \chi + Q\gamma^2[m - 1]\iint dxdy\ \psi\frac{\partial\chi}{\partial y} \\ \text{(iv)}\quad \gamma^2\dfrac{\partial}{\partial t}\displaystyle\iint dxdy\ y\chi = -Q\gamma^2[m - 1]\iint dxdy\ \psi\frac{\partial\chi}{\partial x} \end{array}\right\}. \qquad (2.6)$$

In all numerical computations of (2.4), a finite square domain will be adopted, with boundary conditions of periodicity in x and y on a nondimensional distance $L \gg l$. For this geometry, there are additional boundary integrals in the moment equations (2.6); however, for times even moderately large (i.e., $t \leq 20$ for the parameters typically used below), the final three relations, (ii)–(iv) in (2.6), can be consistently examined neglecting these boundary contributions, because the currents near the boundary are relatively weak and unimportant. These are the only circumstances under which we shall use the moment integrals (2.6).

Initial conditions for the numerical studies are of the form

$$\chi = e^{-r^2}, \quad \psi = \nu\chi, \qquad (2.7)$$

where r $\{=[(x - x_0)^2 + (y - y_0)^2]^{1/2}\}$ is the radial coordinate and (x_0,y_0) is the initial location of the vortex center.[6] The parameter ν is the fractional

[6] In addition, periodicity of ψ and χ is imposed at $x, y = 0, L$. Because these locations are far from (x_0,y_0), this alteration of (2.7) is of small magnitude.

barotropic component of the initial vortex. Note from (2.1) that $\nu = \delta^{1/2}$ defines a compensated vortex (i.e., one with zero lower layer flow). Eqs. (2.4) are symmetric under the interchange of variables, i.e.,

$$\{\psi,\chi,y\} \leftrightarrow \{-\psi, -\chi, -y\}.$$

Therefore, the solutions of (2.4) with an initial positive amplitude in χ, a high-pressure vortex (i.e., one with a sign opposite to that of Gulf Stream rings), can be reinterpreted as a low-pressure vortex by reversing north and south.

A number of other mathematical relations will be used in analyzing the vortex solutions of (2.4), but for brevity their presentation has been assigned to appendices. Various computational relations (finite-difference formulas, resolution scales, etc.) and a list of the numerical cases which are analyzed in this paper are in Appendix A. A linear propagation model (with $Q = \hat{Q} = K_* = 0$) is in Appendix B, and a frictional decay model (with $Q = \hat{Q} = \beta = 0$) is in Appendix C. An asymptotic expansion of (2.4) as $t \to 0$ is in Appendix D.

Finally, a physical interpretation of our solutions can be made for Gulf Stream rings by an appropriate set of values for the dimensional scales in (2.3) and (2.5). We recommend the following:

$$\left.\begin{array}{ll} H_1 = 700 \text{ m}, & H_2 = 4300 \text{ m} \\ l = 60 \text{ km}, & R = 45 \text{ km} \\ f_0 = 0.9 \times 10^{-4} \text{ s}^{-1}, & \beta = 1.7 \times 10^{-11} \text{ m}^{-1} \text{ s}^{-1} \\ V_0 = 0.8 \text{ m s}^{-1},^{7} & g' = 2.7 \times 10^{-2} \text{ m s}^{-2} \end{array}\right\}. \quad (2.8)$$

From these dimensional values we estimate the parameters (2.5) as

$$\left.\begin{array}{ll} Q = 13, & \delta = 0.16 \\ \hat{Q} = 27, & \gamma^2 = 1.8 \end{array}\right\}. \quad (2.9)$$

The only *a priori* statement which we can make about $K_{\text{dimensional}}$ is that K_* probably should be small. *A posteriori* we could make an indirect estimate by fitting our model solutions to the observed decay of rings.

[7] The dimensional azimuthal velocity field v_θ for the vortex (2.7) with $\nu = 0$ is

$$v_\theta(r,z) = -2V_0 r e^{-r^2} F_C(z).$$

$F_C(z)$ was calculated by Flierl (1978) for a realistic North Atlantic mean vertical profile of density. Consistent with (2.2), he found $F_C(0) = 3$ and $F_C(-800 \text{ m}) = 1$; thus,

$$\max_r |v_\theta(z = 0)| = 2.6V_0.$$

For 2 m s^{-1} as an estimate of the maximum surface current of a ring, one obtains the V_0 value in (2.8).

3. A single-mode vortex

The first problem we shall consider is that of an isolated vortex with only a single vertical mode; i.e., the model equation is a truncation of Eq. (2.4) with $m = 1$. Such a model is often referred to as equivalent barotropic. The only parameters of this problem are $\hat{Q}$, γ and K_* from (2.5).

We shall henceforth adopt a set of standard parameter values; *viz.*,

$$\hat{Q} = 10, \quad \gamma^2 = 2, \quad K_* = 5 \times 10^{-4}. \quad (3.1)$$

These represent a vortex which is strongly nonlinear, which has an e-folding radius somewhat larger than the radius of deformation, and which has a slow rate of frictional decay. They also qualitatively represent the parameter regime defined by (2.9), although $\hat{Q}$ in (3.1) is somewhat too small. Because we shall also present solutions with parameters different from (3.1), the consequences of the discrepancies between (3.1) and (2.9) can be assessed *a posteriori*.

A computational solution to the initial value problem for the parameters (3.1) and the Gaussian vortex (2.7) is illustrated in Fig. 1. Over a time interval $\Delta t = 17.3$, the vortex has moved toward the west-southwest, left behind a weak Rossby wave wake [with a characteristic herringbone pattern similar to that shown, for example, in Rhines (1977, Fig. 11) for $\gamma^2 = \hat{Q} = K_* = 0$], decreased somewhat in amplitude, and developed a weak, wavenumber 1 axial asymmetry. On the whole, however, this initially isolated vortex remains an isolated vortex for quite a long period of time (a nondimensional interval of 17.3 corresponds to 196 days for the dimensional values (2.8); the distance traveled is $\Delta s \approx 7.9$ or 470 km; the average rate of translation is $\Delta s/\Delta t \approx 0.46$ or 2.8 cm s^{-1}).

The parameter dependence of the propagation of single-mode vortices is shown in Figs. 2a–2c, which display the trajectories of the position of the maximum in χ for different values of $\hat{Q}$, γ^2, and K_*, respectively.[8] Fig. 2c shows that vortex propagation is insensitive to the frictional decay rate, at least in the $K_* \ll 1$ regime.[9] The propagation does, however, strongly depend on both Q and γ^2.

Flierl (1977) has calculated the propagation rate for a linear, inviscid vortex ($\hat{Q} = K_* = 0$), and his formulas are evaluated for the Gaussian vortex (2.7) in our Appendix B. Initially, the zonal rate has a small westward value, $dx_c/dt = -0.13$ [we define

[8] $\hat{Q}$ and γ are, crudely, measures of the vortex strength and size. However, from (2.5) one can see that both parameters depend on l. Refer to Appendix A (Fig. A1 in particular) for a display of $\hat{Q}$ and γ variations as a function of V_0 and l.

[9] Note, however, that a purely frictional vortex with $\beta = 0$ (Appendix C) is nonpropagating.

(x_c,y_c) as the position of the pressure maximum]. As time increases, this rate increases until it asymptotically approaches the fastest possible westward linear wave speed, $dx/dt = -1/\gamma^2 = -0.5$. The trajectory for $\hat{Q} = 0$ in Fig. 2a has not yet reached this asymptotic value during the time interval plotted. In this linear theory, the meridional rate is zero. Fig. 2a shows that as $\hat{Q}$ increases from zero, the

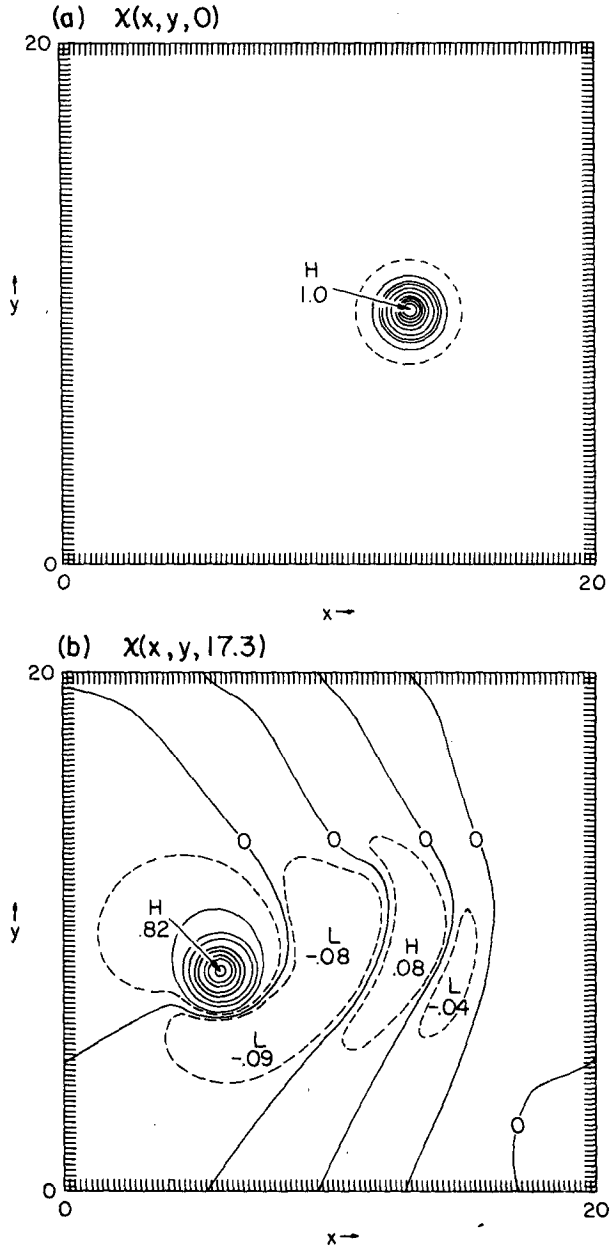

FIG. 1. Contours of $\chi(x,y,t)$ from a numerical solution of the single-mode vortex initial value problem with the standard parameters (3.1): (a) $t = 0$ and (b) $t = 17.3$. The contour interval is 0.1 for the solid line contours; in addition, ± 0.02 contours are drawn with dotted lines.

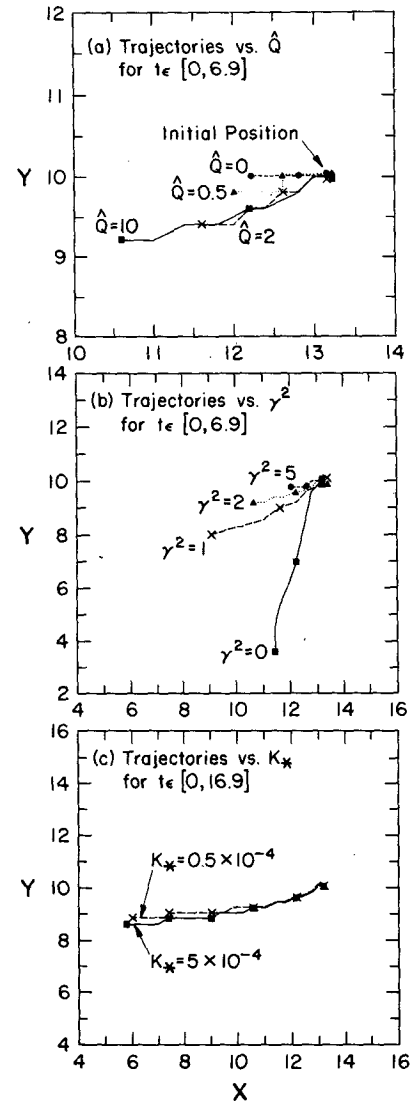

FIG. 2. Trajectories of the positions of the spatial maximum for χ from numerical solutions of the single-mode vortex initial value problem: (a) $\hat{Q}$ variable for $t \in [0,6.9]$, (b) γ^2 variable for $t \in [0,6.9]$, and (c) $K*$ variable for $t \in [0,16.9]$. Except for the parameter being varied in each panel, the values are the standard ones (3.1). The dots indicate positions every $\Delta t = 3.45$. Jumps in the trajectories are due to the finite grid size in the numerical solutions (i.e., $\Delta x = \Delta y = 0.2$).

westward rate increases above the linear value, at least for intermediate times, and the southward rate does as well. In the left-hand panels of Fig. 3a the calculated values of dx_c/dt and dy_c/dt are plotted as a function of $\hat{Q}$ for an intermediate time interval. From these plots we see that 1) $-dx_c/dt$ and $-dy_c/dt$ monotonically increase with $\hat{Q}$; 2) as $\hat{Q} \to \infty$, dx_c/dt and dy_c/dt approach finite values; and 3) it seems likely from these curves that $\hat{Q} = 10$ lies within the large $\hat{Q}$ asymptotic regime for propagation rates. In the case of the zonal rate, the large $\hat{Q}$

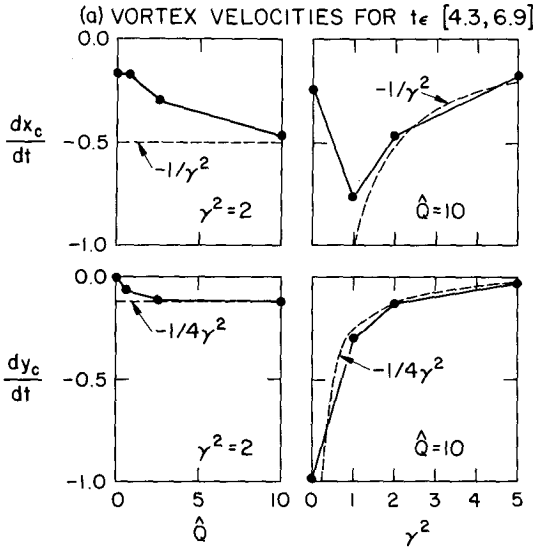

FIG. 3a. Vortex translation velocities as function of $\hat{Q}$ and γ^2 during the time interval $t \in [4.3,6.9]$. These values are finite differences calculated from the trajectories of Figs. 2a and 2b. Also plotted (with dotted lines) are the most negative possible linear wave velocities, $dx/dt = -1/\gamma^2$ (either a phase or a group velocity) and $dy/dt = -1/4\gamma^2$ (a group velocity).

limiting value appears to be the fastest westward linear wave speed $-1/\gamma^2$. For the meridional rate, the limiting value appears to be the fastest southward linear group velocity $-1/4\gamma^2$. The reasons for this are discussed below. Recall that these velocities are made dimensional by the factor βl^2, which equals 0.06 m s^{-1} from Eq. (2.8).

When $\hat{Q}$ is large, the southward rate decreases with increasing γ^2, while the zonal rate has a maximum near $\gamma^2 = 1$ (see Fig. 2b and the right-hand panels of Fig. 3a). For $\gamma^2 \gtrsim 1$ both dx_c/dt and dy_c/dt are close to the bounding curves from linear wave theory. Finally, we note that except perhaps for the purely barotropic vortex ($\gamma^2 = 0$), dy_c/dt tends to increase toward zero as $t \to \infty$, while dx_c/dt does not. In general, the magnitude of dy_c/dt is smaller than that of dx_c/dt except, again, as $\gamma^2 \to 0$. Thus, these vortices will propagate westward for the most part.

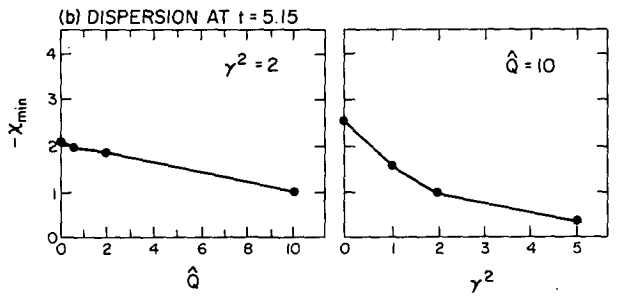

FIG. 3b. Dispersion versus $\hat{Q}$ and γ^2 at a time within the interval of Fig. 3a.

The moment integrals (2.6) indicate how the preceding parameter dependences of propagation are intrinsically coupled to the degree of dispersion which occurs for the vortex. If we define center of mass coordinates $(\bar{x},\bar{y})$ for the vortex center by

$$\left.\begin{aligned} \bar{x} &= \frac{\iint dxdy\, x\chi}{\iint dxdy\, \chi} \\ \bar{y} &= \frac{\iint dxdy\, y\chi}{\iint dxdy\, \chi} \end{aligned}\right\}, \tag{3.2}$$

then for a single-mode vortex in an infinite domain

$$\left.\begin{aligned} \frac{d\bar{x}}{dt} &= -1/\gamma^2 \\ \frac{d\bar{y}}{dt} &= 0 \end{aligned}\right\}. \tag{3.3}$$

That is, the center of mass moves westward at the greatest linear wave speed, and it moves not at all in the meridional direction. From Figs. 1–3, it is clear that the center of the vortex does not always coincide with the center of mass, and this discrepancy can only occur if there is a significant contribution to the moments (3.2) from streamfunction patterns not associated with an axisymmetric, isolated vortex. This departure field in the streamfunction can be defined by

$$\chi' = \chi(x,y,t) - \chi_{\max} \exp[-(x - x_c)^2 - (y - y_c)^2], \tag{3.4}$$

where $\chi_{\max}(t)$ and $[x_c(t),y_c(t)]$ are the maximum streamfunction value and its position at time t, respectively. From (3.2)–(3.4), we can derive the following expressions for the difference between the centers of the vortex and mass:

$$\left.\begin{aligned} x_c - \bar{x} &= -\iint dxdy(x - x_c)\,\chi' \Big/ \iint dxdy\,\chi \\ y_c - \bar{y} &= -\iint dxdy(y - y_c)\,\chi' \Big/ \iint dxdy\,\chi \end{aligned}\right\}, \tag{3.5}$$

where, from (2.6), the denominators are constants in time. If the initial vortex simply propagated and uniformly decayed in time, then χ' would be zero and $(\bar{x},\bar{y})$ would equal (x_c,y_c). One can also see from (3.5) that positive χ' values to the west of x_c (north of y_c) and negative χ' values to the east of x_c (south of y_c) allow x_c to be to the east of $\bar{x}$ (y_c south of $\bar{y}$).

In a linear vortex solution, $-1/\gamma^2 \leq dx_c/dt < 0$

and $dy_c/dt = 0$. For such a case χ' is even symmetric about y_c, hence $\bar{y} = y_c$ [see, e.g., Rhines (1977, Fig. 11) or Flierl (1977, Fig. 3.1)]. On the other hand, χ' has a positive center to the west of the main vortex and a negative one to the east; these centers allow dx_c/dt to be more positive than $d\bar{x}/dt = -1/\gamma^2$. As $t \to \infty$, the main vortex overtakes the leading positive center in χ', and to the east χ' exhibits an alternating sequence of bands, the Rossby wave wake, whose integral contribution to $\bar{x}$ in (3.2) is negligible; hence $dx_c/dt \to d\bar{x}/dt$. For significant nonlinearity, however, the departure field is quite different: its amplitude is much smaller and there is significant north-south asymmetry about y_c in χ'. Fig. 4 shows χ' at $t = 5.2$ and 17.3 for the standard parameters (3.1). The leading positive center has now shifted more to the north of the main vortex [and encloses the central position (x_c, y_c) as well] and the trailing positive and negative centers are now displaced to the north or south, respectively, of y_c. As a consequence, dx_c/dt is much closer to $d\bar{x}/dt$, and dy_c/dt has a significant southward component.

One can see from Figs. 1 and 4 that the largest amplitude in the streamfunction field outside the main vortex is associated with the first trailing low-pressure center to the east. Thus, its amplitude, defined as minus the spatial minimum value of χ [i.e., $-\chi_{\min}(t)$], is a measure of the degree of dispersion which has occurred by time t. Fig. 3b is a plot of this amplitude versus $\hat{Q}$ and γ^2. Dispersion decreases with increases in either parameter, when they are varied about their standard values (3.1). For linear solutions ($\hat{Q} = 0$), it is well known that dispersion decreases with increasing vortex size, since the group and phase velocities become independent of wavenumber as $\gamma^2 \to \infty$. Nonlinearity also inhibits dispersion.

One can interpret the meridional χ' asymmetry, hence the meridional vortex motion as above, by the following argument. The initial dispersive tendency for a vortex is primarily due to linear, inviscid processes (see Appendix D), and the dispersion pattern initially consists of a positive χ' center to the west of the vortex and a negative one to the east. The circulation of the main vortex is clockwise; hence these χ' centers are advected clockwise. Such displacements reduce the magnitude of the $(x - x_c)\chi'$ moment and increase the magnitude of the $(y - y_c)\chi'$ moment, which lead through Eqs. (3.5) to a westward propagation closer to $-1/\gamma^2$ and a net southward propagation. An alternative, more mechanistic interpretation of the southward motion of the vortex—one which does not refer to the moment integrals—is that the leading and trailing dispersion centers have secondary circulations which both act to advect the main vortex southward.

Neither of the preceding arguments determine a rate for the southward vortex propagation, yet from Fig. 3 it is clear that $dy_c/dt \approx -1/4\gamma^2$ accurately represents the numerical solutions for γ, $\hat{Q} \gtrsim 1$. The linear waves associated with the $m = 1$, $\hat{Q} = 0$, $K_* = 0$ form of (2.4b) have a nondimensional dispersion relation

$$\omega = -\frac{k}{k^2 + l^2 + \gamma^2}, \tag{3.6}$$

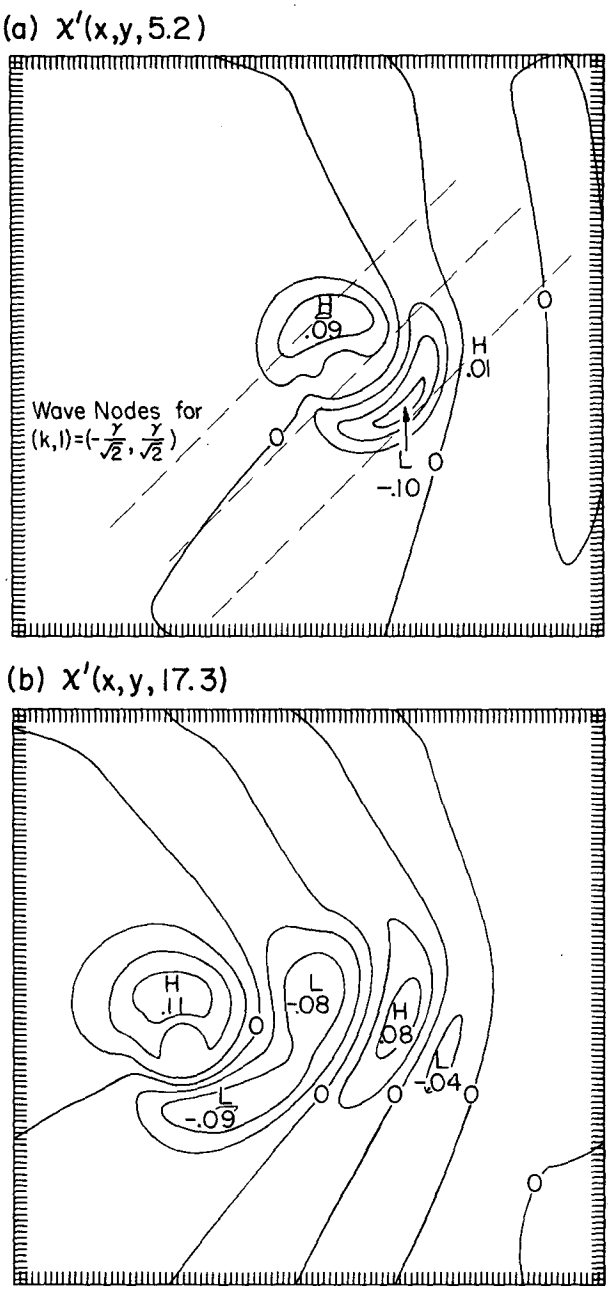

FIG. 4. The departure fields (3.4) for the standard case numerical solution at (a) $t = 5.2$ and (b) $t = 17.3$ (see Fig. 1b for χ at this latter time). The contour interval is 0.03. Also drawn on panel (a) are nodal lines for a plane wave with the indicated wavenumber (see text for discussion).

where (k,l) is the vector wavenumber and ω is the frequency. For such waves the meridional group velocity, $c_g^{(y)} \equiv \partial\omega/\partial l$, lies within the range $(-1/4\gamma^2, 1/4\gamma^2)$. From (3.5) and Fig. 3, therefore, we can deduce the relation

$$\frac{d/dt \iint dxdy(y - y_c)\chi'}{\iint dxdy\ \chi} \approx \max_{(k,l)} |c_g^{(y)}|. \quad (3.7)$$

By the usual interpretation of nearly monochromatic wavepackets, one would expect a small amplitude disturbance with (k,l) equal to either $(-\gamma/\sqrt{2}, \gamma/\sqrt{2})$ or $(-\gamma/\sqrt{2}, -\gamma/\sqrt{2})$ to move meridionally with a speed equal to $\max|c_g^{(y)}|$. From Fig. 4a, one can see that χ' is of small amplitude (so that one might reasonably expect its evolution to be described by linear wave theory) and has a significant component near the first of the two wavenumbers above at $t = 5.2$, hence with group velocities near $c_g^{(y)} = -1/4\gamma^2$. The near match of the group velocity of the χ' pattern with the propagation velocity of the main vortex which generates it allows for a continual intensification of this pattern at the rate implied by (3.7). The southward vortex propagation rate could be no greater because the linearly propagating χ' structure would be unable to keep up with the vortex and thus would not have its y moment intensify as required to maintain southward motion. Of course, χ' is not solely the plane wave with maximum group velocity. Its structure becomes more complicated with time (as indicated in Fig. 4b) and the right-hand side of (3.7) becomes an upper bound on the southward vortex propagation rate. Note from Fig. 2c the decrease of $|dy_c/dt|$ at longer times.

In summary, strong dispersion (when $\hat{Q} \to 0$ for moderate values of γ^2 or when $\gamma^2 \to 0$ for any $\hat{Q}$) allows the zonal propagation rate to be much slower than the fastest linear wave speed. If it occurs symmetrically in y (as when $\hat{Q} \to 0$), then there is no meridional motion of the vortex. Weak dispersion (when either $\hat{Q}$ becomes large for finite γ^2 or when $\gamma^2 \to \infty$) is weak enough to allow $\bar{x} \approx x_c$ yet strong enough to allow significant meridional motion when the dispersion is asymmetric (as when $\hat{Q}$ is large). For sufficiently large t, the vortex amplitude becomes small and the dispersion field, for all γ^2 and $\hat{Q}$ values, has little integral contribution to the moment integrals (3.3) and (3.5). Thus, $dx_c/dt \to -1/\gamma^2$ and $dy_c/dt \to 0$ as $t \to \infty$.

A possible interpretation of the north-south motion of the vortex is that it reflects a tendency to return to the rest latitude (i.e., the value of y where a particle retains its initial value of potential vorticity but with no motion). It is evident, however, that this does not occur completely. For example, the particle initially in the center has a potential vorticity

$$(\nabla^2 - \gamma^2)\chi|_{r=0} + \hat{Q}^{-1}y_0 = -4 - \gamma^2 + \hat{Q}^{-1}y_0,$$

corresponding to a rest latitude

$$y_r = y_0 - \hat{Q}(\gamma^2 + 4)$$

or a displacement of 60 units southward for the standard case, assuming the particle initially in the center remains in the vortex (even if it does come out, it is hard to imagine that it is pushed very much further south than the eddy). Though the final latitude of the vortex cannot be accurately determined, Fig. 2c would certainly suggest a net displacement of only about 2 units. Friction also contributes to this discrepancy.

Another technique for distinguishing between several influences in vortex evolution is by means of an asymptotic expansion as $t \to 0$. The terms in the expansion are defined in Appendix D, and the more prominent ones are displayed in Fig. 5. The initial baroclinic vortex (2.7) is shown in Fig. 5a. The $O(t)$ streamfunction tendency terms $\chi_{1\beta}$ due to the β-effect and χ_{1K} due to the friction, are shown in Figs. 5b and 5c. Because of the axial symmetry of $\chi(x,y,0)$ there are no nonlinear effects at $O(t)$. $\chi_{1\beta}$ has a two-cell structure, with a positive center to the west of the initial vortex position and a negative center to the east. This can be interpreted as primarily a tendency for westward propagation of the vortex. Note that $\chi_{1\beta} = 0$ at $[x_c(0),y_c(0)]$; there is no $O(t)$ tendency for a decrease in maximum amplitude of the vortex due to the β-effect [cf., equation (B3)]. If there were a purely westward propagating solution

$$\chi\left[x - \int_0^t V(t')dt', y\right],$$

then at $t = 0$, $\chi_t = -V(0)\chi_x(x,y)$. For a value of $V(0) = -0.135$ (this is the value which correctly describes the initial propagation of the vortex center —see Appendix B), one can compare $\chi_{1\beta}$ with $+2V(0)(x - x_0)\exp[-(x - x_0)^2 - (y - y_0)^2]$ to evaluate the extent to which $\chi_{1\beta}$ is pure propagation. A cross-sectional comparison along the x axis is shown in Fig. 6. $\chi_{1\beta}$ attains a larger extremum farther from the vortex center and decays more slowly for large distances than does the pure propagation tendency $+2V(0)(x - x_0)\exp[-(x - x_0)^2]$. The choice made for $V(0)$ requires equal slopes for the two curves at the origin; some other choice would change the amplitude of the pure propagation curve, but its extent would not match that of $\chi_{1\beta}$. Thus, $\chi_{1\beta}$ is not entirely a westward propagation tendency; it also represents a β-induced dispersion [i.e., a positive (negative) center developing ahead

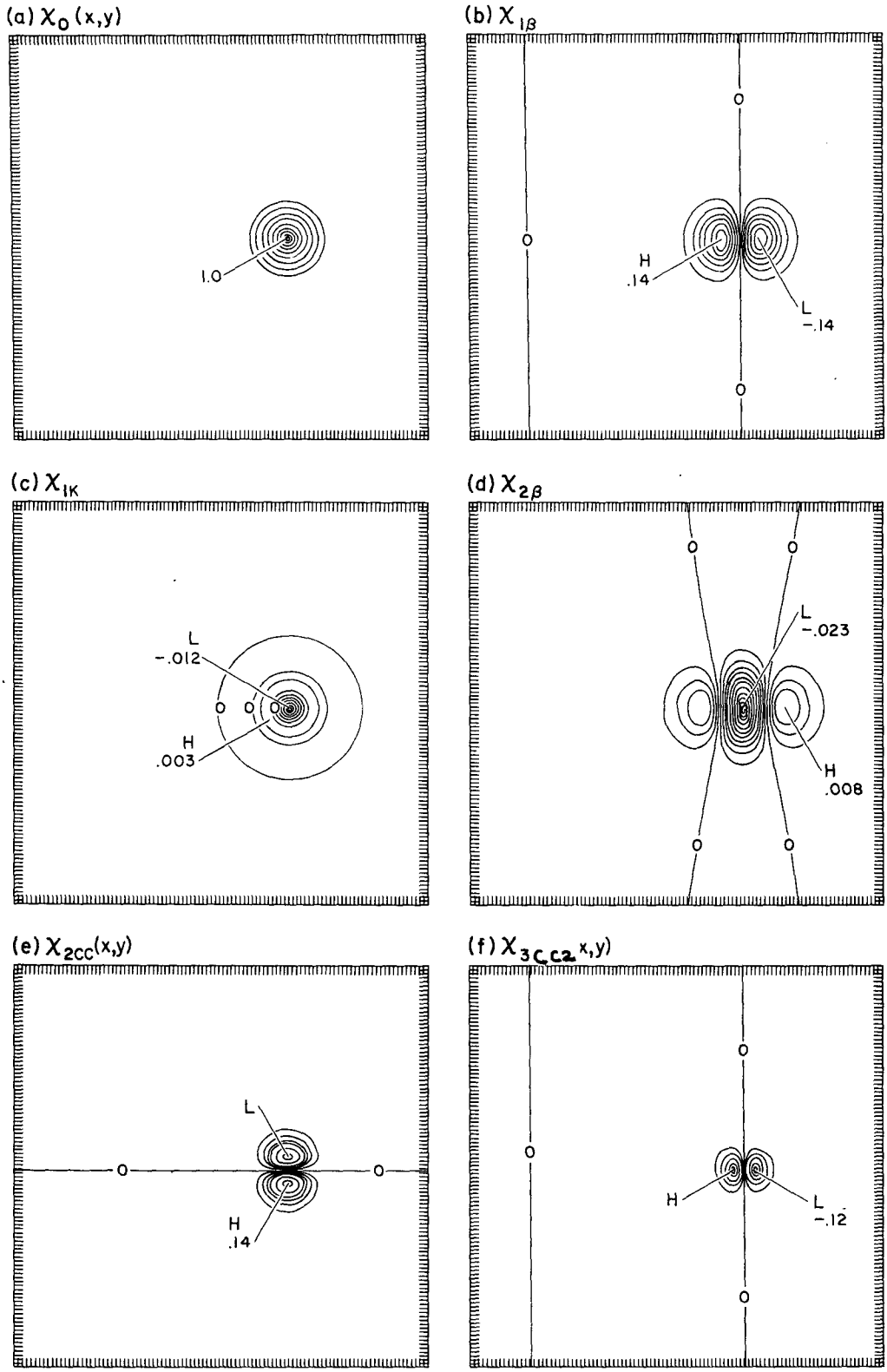

FIG. 5. Selected spatial coefficients of power of t in a small t expansion for a single-mode vortex with the standard parameters (3.1). The coefficients are defined in Eqs. (D1), (D3), (D5) and (D7). Contour intervals are 0.1 for panel (a), 0.02 for panels (b), (e) and (f), and 0.002 for panels (c) and (d).

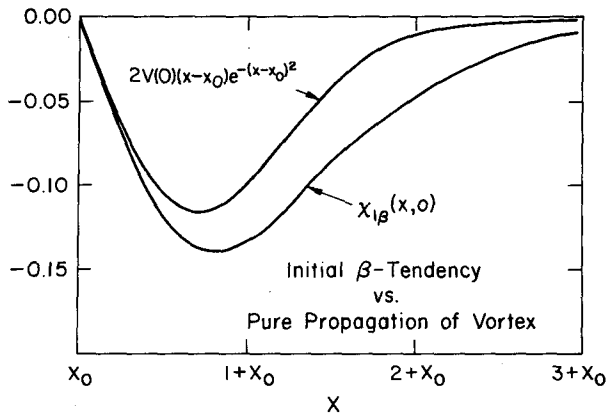

FIG. 6. A comparison of the $O(t)$ streamfunction tendency due to the β-effect, $\chi_{1\beta}$, with the functional form with which a tendency for pure vortex propagation would occur at $O(t)$. $V(0) = -0.135$ here (see Appendix B). Parameter values are given in Eq. (3.1).

of (behind) the main vortex as discussed above with reference to the integral moments].

χ_{1K}, the frictional tendency at $O(t)$, has a central region of small negative values and thus represents decay of the maximum amplitude of the vortex. Note, also, that it has a radial zero crossing at $r \approx 0.7$. Since this radius is smaller than that of the main vortex, the frictional tendency also includes a general flattening of the initially Gaussian vortex. This tendency is reflected at later times in χ' as a generally positive region about the vortex center (see Fig. 4).

$\chi_{2\beta}$ represents an $O(t^2)$ β tendency. It is shown in Fig. 5d. Its central negative values represent a combination of propagation and decay of the central vortex amplitude,[10] while its leading and trailing positive centers represent further dispersion and westward propagation. The terms χ_{2CC} and $\chi_{3C\,C2}$ are due to nonlinear self-interactions of the initially propagating and dispersing vortex. They are also the dominant tendencies at $O(t^2)$ and $O(t^3)$, respectively (see Table D1). Both have an antisymmetric, two-center structure (see Figs. 5e and 5f), with which we have previously identified propagation tendencies. χ_{2CC} has its positive center to the south of the vortex center, while $\chi_{3C\,C2}$ has its positive center to the west. Thus, nonlinearities allow for a southward and augmented westward propagation relative to the β-effect alone. Because the spatial scales of χ_{2CC} and $\chi_{3C\,C2}$ are slightly smaller than that of the main vortex (Fig. 5a)—and certainly smaller than that of $\chi_{1\beta}$ in Fig. 5b—they represent little dispersion and, in the case of $\chi_{3C\,C2}$, even a weak tendency to cancel the dispersion of $\chi_{1\beta}$.

Since we know from Fig. 1 that the single-mode vortex solution retains much of the character of its initial state, we can qualitatively apply the small-time tendencies to an interpretation of larger time behavior. This is further illustrated in Fig. 7, which shows χ and its tendencies due to various terms in the potential vorticity equation (2.4b) at a moderately large time, $t = 5.2$ [from (2.8), this corresponds to 59 days]. The β term (Fig. 7b) represents a westward propagation and dispersion tendency; the frictional term (Fig. 7c) represents a decay and flattening of the vortex; the nonlinear term (Fig. 7d) represents a southwestward propagation at a rate about twice that due to the β term. Note in particular that there is little streamfunction tendency at the vortex center except that due to friction.

The final feature of the single-mode vortex solution which we shall address here is the rate of decay of its maximum amplitude $\chi_{\max}(t)$. For the standard parameters (3.1), this function is plotted in Fig. 8. $\chi_{\max}(t)$ is monotonically decreasing with time, with a somewhat slower decay rate for larger times. Also shown in Fig. 8 are two extreme solutions for comparison. One is from the linear inviscid solution [Eq. (B1)]; except for small values of t ($\lesssim 2$), this solution has a much smaller vortex amplitude than does the standard solution. Thus, the large nonlinearity of the standard solution significantly slows the rate of vortex decay due to linear wave dispersion. The other comparison solution is for pure frictional decay with $\beta = 0$ [Eq. (C1)]. Its value for $\chi_{\max}$ is everywhere larger than the standard one, implying that moderate dispersion does occur in the general case even for large nonlinearity; however, the two curves are close enough that we can conclude that a major fraction (~79% by $t = 17.3$) of the vortex decay in the standard case is due solely to the action of friction.

This conclusion is reinforced by Fig. 9c, which shows $\chi_{\max}(t)$ for two different values of K_*. The decay rate is much smaller for K_* reduced by an order of magnitude from the standard value. If we compare the smaller K_* solution with a corresponding purely frictional solution (not plotted), then we can conclude that 53% of the decay is frictional by $t = 17.3$, even for this very small value of K_*. For a single mode vortex, therefore, the rate of

[10] Note that the streamfunction tendency at the initial location of the vortex, $(x_0,y_0) = [x_c(0),y_c(0)]$, is proportional at $O(t)$ to $\chi_{2\beta}(x_0,y_0)$, which arises primarily through the linear inviscid terms alone:

$$\partial/\partial t\chi(x_0,y_0,t) = \ldots - 2t\chi_{2\beta}(x_0,y_0) + \ldots = -0.046t + \ldots,$$

where the numerical coefficient is taken from Fig. 5d. In contrast, the linear, inviscid vortex central tendency [Eq. (B3)] has a slower rate of decay at this same order,

$$d/dt\chi_{\max}(t) \equiv d/dt\chi(x_c(t),y_c(t),t) = -0.014t + O(t^2),$$

where the numerical coefficient is for $\gamma^2 = 2$. Thus, the former tendency is more than simple vortex decay, and also represents a decrease of amplitude due to the motion of the vortex center to the west of (x_0,y_0).

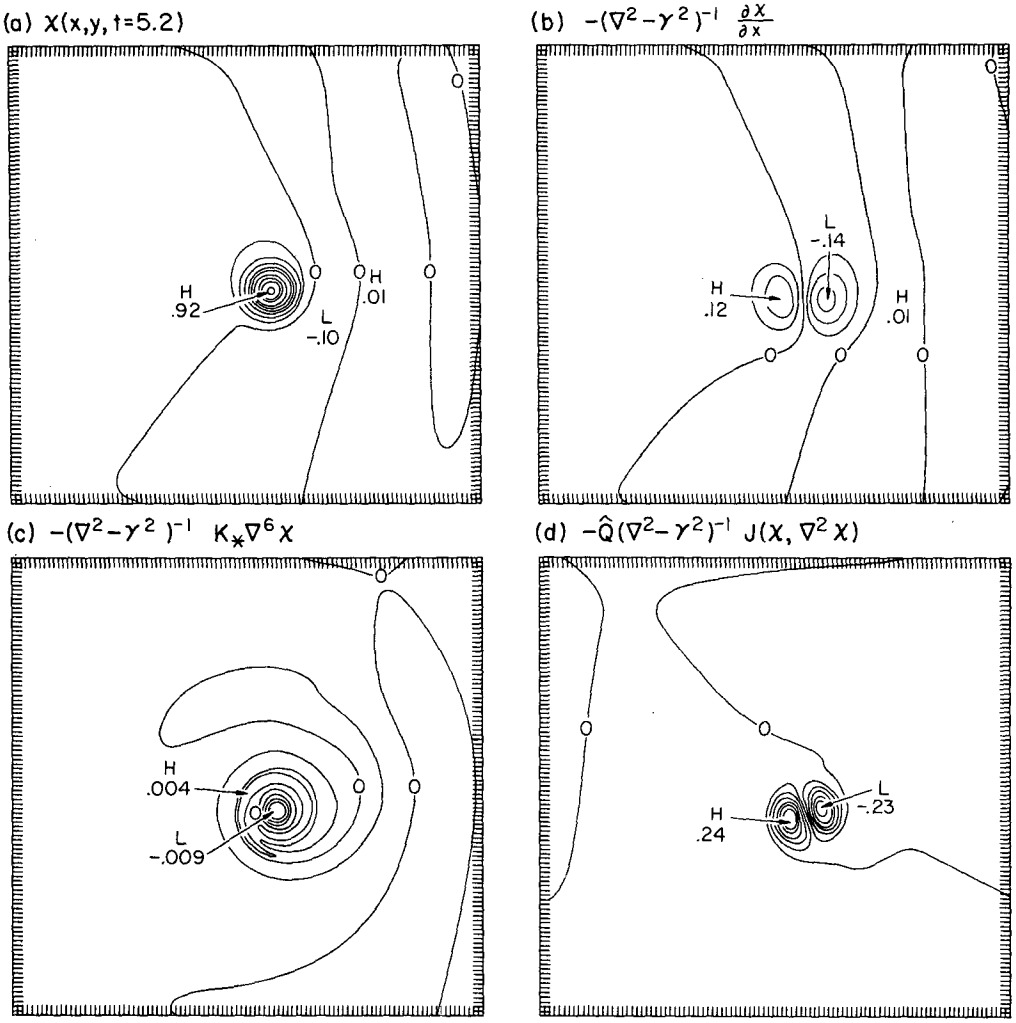

FIG. 7. (a) $\chi(x,y)$ at $t = 5.2$; (b)–(d) streamfunction tendencies due to the indicated terms in the potential vorticity equation (2.4b). Parameter values are given in Eq. (3.1). Contour intervals are 0.1 for (a), 0.04 for (b) and (d), and 0.002 for (c).

amplitude decay is essentially governed by the frictional rate when Q and γ^2 are large.

We can also compare the decay rate to the estimates of Parker (1971) or Cheney and Richardson (1977) that the thermocline subsides at 0.6 or 0.4 m day^{-1}, respectively. Our initial state corresponds to about a 140 m displacement. The decay rates in Fig. 8 for the standard case are thus 0.1–0.2 m day^{-1}—quite small. This discrepancy is probably accounted for by transfers along various vertical modes (see Fig. 13), though the value of the frictional coefficient is also relevant.

Other parameter dependences for $\chi_{max}(t)$ are shown in Figs. 9a and 9b. In the former we see that χ_{max} decreases more slowly with t as $\hat{Q}$ increases, and in the latter we see that χ_{max} decreases more slowly as γ^2 increases. Both of these trends are consistent with dispersion decreasing with increasing γ^2 and $\hat{Q}$.

4. A baroclinic vortex in a two-mode model

The calculations of the preceding section can be extended to the full two-mode model equations (2.4ab) by setting $m = 2$. If initially the vortex is purely baroclinic [i.e., $\nu = 0$ in (2.7)], then the nondimensional parameters of the problem are $\hat{Q}$, δ (or Q), γ and K_*.

First we consider a numerical solution for the standard parameters (3.1) plus $\delta = 0.16$ ($Q = 4.76$). Contour plots of ψ and χ for various times are shown in Fig. 10. Initially (Fig. 10b), χ evolves much as in the single-mode solution (i.e., it moves southwestward with a dispersion pattern of a positive center to the northwest and a negative one to the southeast), while the ψ pattern (Fig. 10a) is a vortex pair spinning up from rest. At an intermediate time of $t \approx 9.2$ or 104 days (Figs. 10c and 10d), the rate of intensification of the barotropic vortex pair

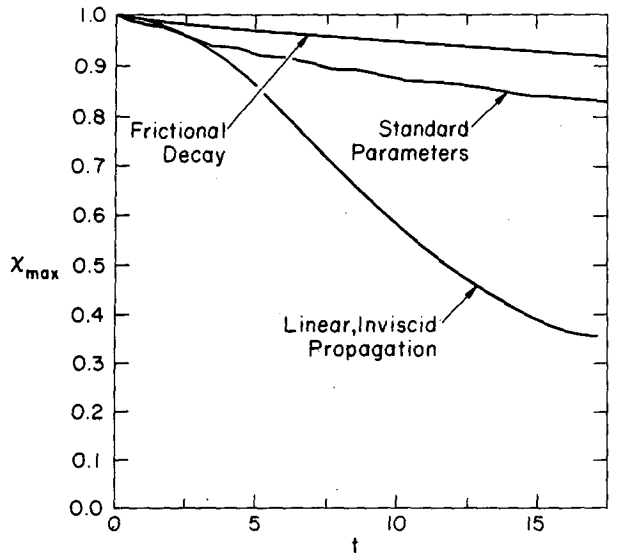

FIG. 8. The evolution of the streamfunction maximum for a single-mode vortex with the standard parameters (3.1). Also shown for comparison are $\chi_{max}(t)$ from a purely frictional model solution [Eq. (C1)] and from a linear, inviscid model solution [Eq. (B1)].

greatly slows and the westward motion of the baroclinic vortex is arrested. At later times, the baroclinic vortex returns to a southwestward propagation (Figs. 10g and 10h), while the barotropic centers separate and radiate Rossby waves (Fig. 10e) and eventually become highly meridionally asymmetric (Fig. 10g). The baroclinic field retains the character of an isolated vortex, while the barotropic one tends toward a uniform eddy far field. Trajectories for the various eddy centers are shown in Fig. 11a. Initially the baroclinic center lies between the two barotropic centers, but it soon shifts southward over the positive barotropic eddy as all three centers begin moving eastward. After there is a sufficient southward displacement of the positive centers, separating them from the negative barotropic vortex, they begin a southwestward motion, while the negative barotropic vortex moves northwestward (recall from Section 3 that isolated, nonlinear, single-mode eddies, whatever the value of γ, move southwest if they have a positive pressure extremum and northwest if negative). The amplitude of the eddy center (Fig. 11b) shows an initial weakening (for $t \lesssim 6$) followed by a longer period of much slower changes. This can also be seen in an integral measure in Fig. 12, where the nonlinear modal energy conversion rate ϵ is plotted against time. ϵ is defined by

$$\epsilon \equiv Q \int_0^L \int_0^L dxdy\ \psi J(\chi, \nabla^2\chi), \tag{4.1}$$

and it can be interpreted as a source of barotropic energy at the expense of baroclinic as follows. From (2.4) with $m = 2$, we can derive modal energy

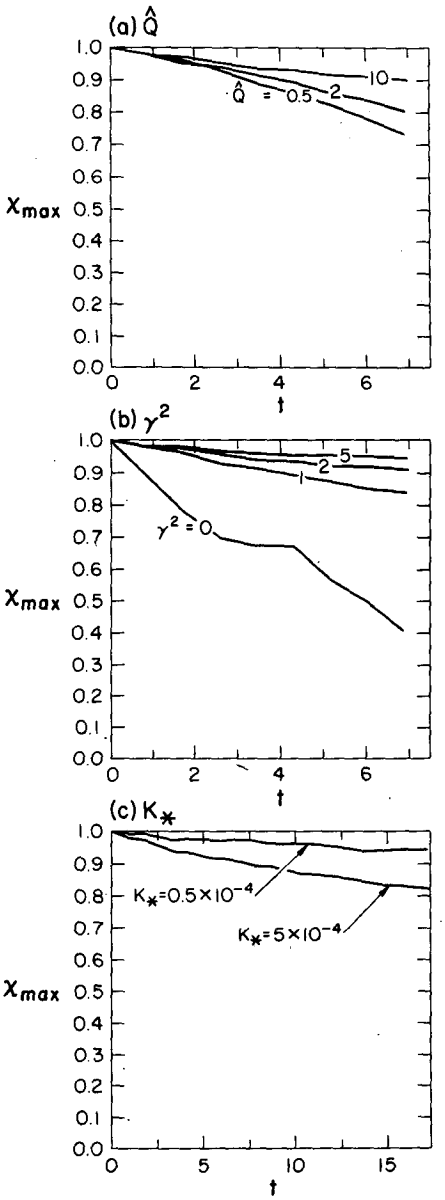

FIG. 9. Parameter variations for $\chi_{max}(t)$: (a) variable $\hat{Q}$, (b) variable γ^2, and (c) variable K_*. Except for the parameter being varied, the values are the standard ones (3.1).

equations

$$\left.\begin{aligned} &\frac{\partial}{\partial t}\left[\frac{1}{2}\iint dxdy(\nabla\psi)^2\right] \\ &\quad = \epsilon - K_* \iint dxdy[\nabla(\nabla^2\psi)]^2 \\ &\frac{\partial}{\partial t}\left[\frac{1}{2}\iint dxdy[(\nabla\chi)^2 + \gamma^2\chi^2]\right] \\ &\quad = -\epsilon - K_* \iint dxdy[\nabla(\nabla^2\chi)]^2 \end{aligned}\right\}. \tag{4.2}$$

For the numerical solution under discussion, ϵ has a strong positive peak for $t \leq 6$ and weaker positive values for $t \in [6,40]$.

Various parameter variations are shown for $\chi_{max}(t)$, $x_c(t)$ and $y_c(t)$ in Figs. 13 and 14. As a function of vertical mode number m, the *initial* rate of vortex decay is much greater when m is larger and, as described above, there can be an arrest to westward propagation when $m \simeq 2$ (Fig. 13a). For weaker nonlinearity (see Figs. 14a and 14c), the arrest need not occur (the barotropic vortex pair is not spun up rapidly enough to cause the arrest—see the $t \to 0$ analysis below), and the rate of baroclinic vortex decay is initially slower (because the modal energy conversion rate ϵ is much less) but eventually more rapid (vortex dispersion is greater for smaller Q). For a larger baroclinic vortex (Figs. 14b and 14d), the arrest can be more systematic, even to the point of persistent eastward propagation, and the rate of amplitude decay is smaller (which is consistent with Fig. 9b).

Two of the most prominent differences between these two-mode and the one-mode solutions are the spinup of the barotropic vortex pair and the tendency for eastward propagation of the baroclinic vortex due to modal coupling. Both of these features can be seen in the small t asymptotic solutions (Appendix D). Each of the tendencies shown in Fig. 5 for the single-mode solution are applicable to the two-mode, $\nu = 0$ case as well (see Table D2). In addition, there are modal coupling terms, the larger ones of which are shown in Fig. 15. The leading order barotropic term occurs at $O(t^2)$ due primarily to baroclinic advection of baroclinic vorticity associated with the $O(t)$ linear wave dispersion. This term is ψ_{2CC} from Eq. (D4), and it is plotted in Fig. 15a. Its structure is that of a meridionally antisymmetric vortex pair, similar to ψ ($t = 1.5$) in Fig. 10a but for a small clockwise rotation of the pattern in the latter. Fig. 15b shows the dominant $O(t^3)$ barotropic term, $\psi_{3C\,C2}$ from (D6), which is such as to give this clockwise rotation when added to ψ_{2CC}. The leading order barotropic back interaction on the baroclinic vortex is $\chi_{3C\,T1}$ from (D7), which is shown in Fig. 5c. It has the antisymmetric two-center pattern which we identified with propagation of the main vortex in Fig. 5. Unlike χ_{1B} and $\chi_{3C\,C2}$ (Figs. 5b and 5f), however, $\chi_{3C\,T1}$ has its positive center to the east and thus represents an eastward propagation tendency. This is the small time manifestation of the propagation arrest shown in Fig. 11a. Even though its amplitude is relatively small in this asymptotic expansion (see Table D2), its effect can be quite important for finite times if Q and γ are large enough (e.g., see Figs. 14a and 14b).

The moment equations (2.6) have additional terms, compared to Eqs. (3.3), due to modal coupling when $m = 2$. With reference to the vortex configurations which occur in Figs. 10 and 11, we note the following influences of these additional terms on $d\bar{x}/dt$ and $d\bar{y}/dt$: (i) for a meridionally antisymmetric ψ pattern centered beneath χ_{max} (as in Fig. 15a), eastward propagation is increased and meridional propagation is unaltered; (ii) for a moderate clockwise rotation of the above ψ pattern (as in Fig. 10a), the eastward propagation tendency is less strong and there is a southward tendency as well; (iii) for a small southward relative displacement of the baroclinic vortex center (as in Fig. 11a for $t \leq 6$), the tendencies in (i) and (ii) are relatively weaker; (iv) for concentric barotropic and baroclinic axisymmetric, positive vortices (as, crudely, is shown in Fig. 11a for $t \geq 18$), there is no modal coupling influence on center of mass propagation; (v) for the positive barotropic center in (iv) slightly displaced to the northwest (more precisely, as shown in Fig. 11a for $t \geq 20$), the modal coupling propagation tendency is westward and southward; and (vi) for a negative barotropic center to the east of χ_{max} (as appears weakly in Fig. 10g), the propagation tendency is southward. These various influences are reflected in the motion of the baroclinic vortex in its early westward arrest [(i), (ii) and (iii) above], its shift from being centered between the barotropic vortex pair to being more concentric with the southern high center in ψ [(ii) above], and its later southwestward motion [(iv), (v) and (vi) above].

Compared to the $m = 1$ solution (see Fig. 13a), the two-mode vortex, in its latest stages, moves much more rapidly southward and slightly more rapidly westward. The former is clearly due to the presence of positive and negative barotropic centers, respectively, to the west and east of the main vortex. The latter is probably the result of a competition between weaker westward propagation due to a smaller vortex amplitude in the two-mode case (see Figs. 3a and 13b) and greater westward propagation due to the positive barotropic center relatively displaced to the north. A dimensional evaluation of the $m = 2$ velocities, based on Eq. (2.8), yields westward and southward values of 3 and 2 cm s^{-1}, respectively.

In the initial stages of evolution shown in Figs. 10–12, the baroclinic vortex approaches a solitary eddy solution known as a vortical modon (Flierl *et al.*, 1979). This solution consists of an eastward propagating, permanent form, barotropic vortex pair (with a negative center north of a positive center) accompanied by a passive rider which is an axisymmetric baroclinic mode vortex of arbitrary amplitude. For a vortical modon, there exists a particular relationship between the barotropic streamfunction magnitude $\Delta\psi_m$ (which we define as $\max\psi - \min\psi$), the distance between vortex centers Δy_m, and the rate of eastward propagation of the modon dx_m/dt. For comparison with modon theory, we renormalize

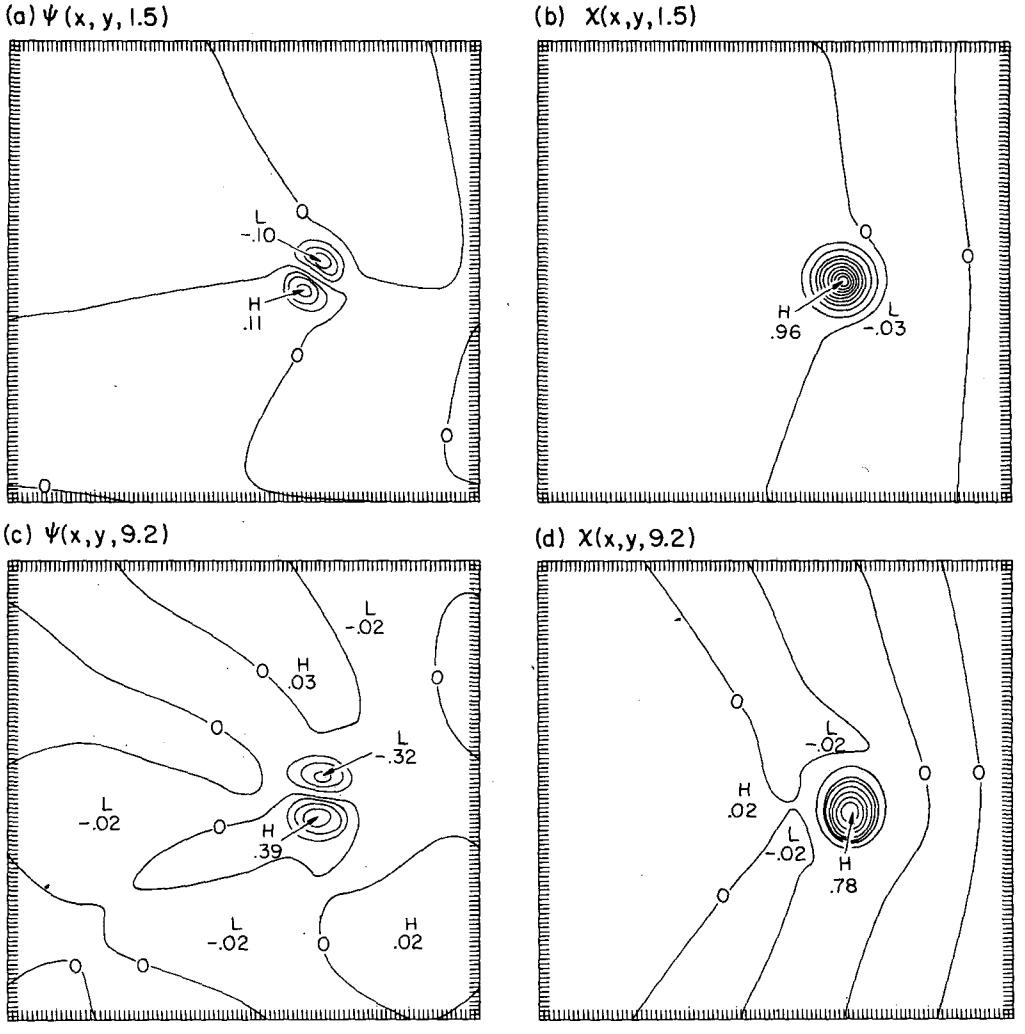

FIG. 10. Barotropic and baroclinic streamfunction patterns at various times from a numerical solution for the parameters (3.1) plus $\nu = 0$, $m = 2$ and $\delta = 0.16$. The contour interval is 0.1 for all plots except (a), where it is 0.03.

the preceding quantities as follows:

$$\left.\begin{aligned} M &\equiv \tfrac{1}{2}Q\gamma^2\Delta\psi_m \\ \hat{I} &\equiv \tfrac{1}{2}\gamma\Delta y_m \\ C &\equiv \gamma^2\frac{dx_m}{dt} \end{aligned}\right\}. \tag{4.3}$$

Verifying that the numerical initial value solution of Fig. 10 closely approaches a vortical modon can be accomplished as follows. For $2 \leqslant t \leqslant 4$, the ψ and χ fields have spatial patterns qualitatively similar to those of vortical modons. Furthermore, we can estimate from Figs. 10–11 the following quantitative values:

$$\left.\begin{aligned} \Delta\psi_m &= 0.42 \pm 0.12 \\ \Delta y_m &= 1.4 \pm 0.1 \\ \frac{dx_m}{dt} &= 0.15 \pm 0.03 \end{aligned}\right\}. \tag{4.4}$$

From (4.3), these values correspond to

$$\left.\begin{aligned} M &= 2\text{–}3.7 \\ \hat{I} &= 0.93\text{–}1.07 \\ C &= 0.24\text{–}0.36 \end{aligned}\right\}. \tag{4.5}$$

Fig. 16 shows the theoretical property relations for a vortical modon, together with the ranges in property values (4.5) for the numerical solution. It can be seen that these ranges have a finite area of common intersection, which implies that, at the level of idealization of vortical modons represented by the scales (4.3), the baroclinic vortex evolution passes through such a solution state. Obviously, it does not persist in this solution state. On the other hand, vortical modons, while valid steady-state solutions of an inviscid, two-mode model, are known to be strongly unstable to infinitesimal perturbations (Flierl and

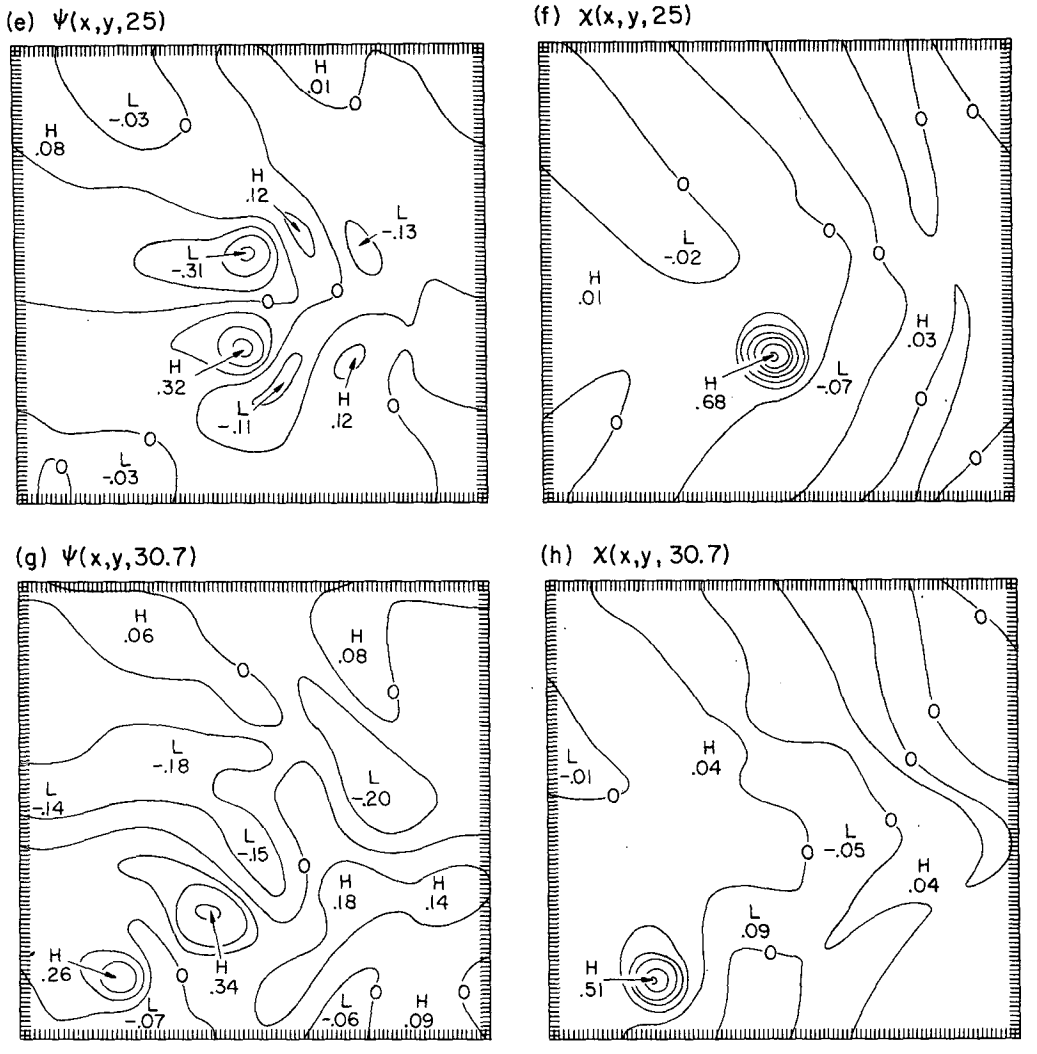

FIG. 10. (*Continued*)

McWilliams, 1979) whenever the baroclinic streamfunction amplitude is comparable to that of the barotropic streamfunction.

For times later than the approximate modon state, the standard parameter, two-mode vortex solution is approximately compensated (i.e., the lower layer expression of the main vortex is quite weak). This feature [also remarked upon by Mied (1978)] can be seen in Figs. 10e–10h and 11b, where the ratio of barotropic and baroclinic streamfunction amplitudes in the main vortex is approximately $\delta^{1/2} = 0.4$; from (2.1) this implies $\psi_2 \approx 0$. Because compensation is a reasonably general property of two-mode vortices, this issue is more fully discussed in the next section.

5. Mixed-mode vortices

In this section we shall examine solutions for two-mode vortices with a nonzero initial barotropic component [i.e., $m = 2$ and $\nu \neq 0$ in (2.4) and (2.7)]. It was shown in Section 4 that even a purely baroclinic initial vortex develops a barotropic companion vortex which is approximately compensating at depth, and here we shall explore this tendency further.

Streamfunction patterns are shown in Fig. 17 for an initially compensated vortex. The vortex propagates to the southwest, with both modal components moving together. The dispersion is relatively much greater in the barotropic field, although the vertical structure remains approximately compensated (e.g., $\max\psi/\max\chi = 0.39$ at $t = 9.2$, and ψ_2 in Fig. 17f shows little evidence of the main vortex). The energy loss from the main vortex by barotropic dispersion is consistent with continuing compensation. The dispersion loss is balanced partly by a transfer of baroclinic energy through nonlinear model coupling, and partly by the barotropic component of the vortex which adjusts to a smaller energy by a shrinking of

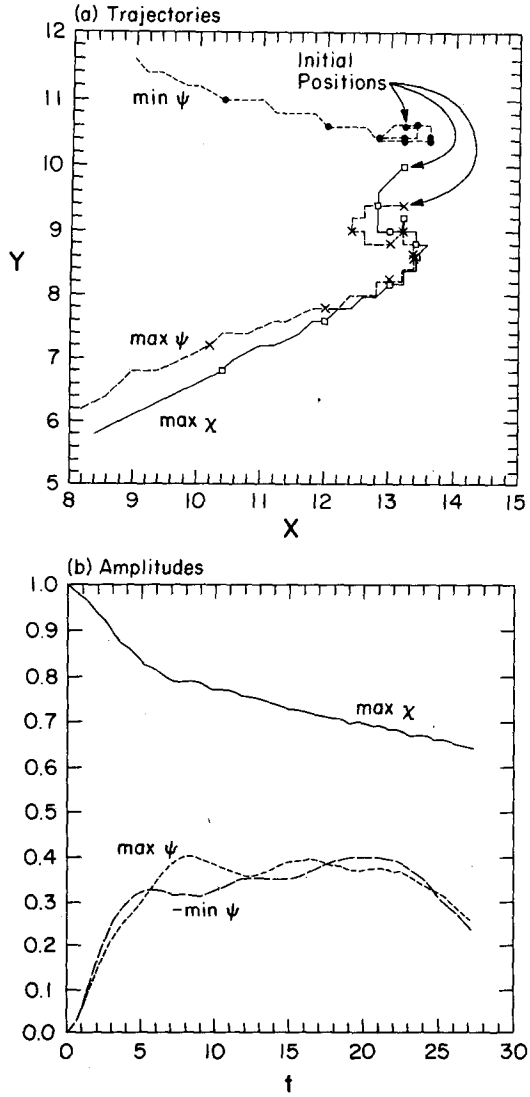

FIG. 11. Trajectory (a) and amplitude (b) plots for three streamfunction extrema from the numerical solution described in Fig. 10. In (a), small squares demark time intervals of $\Delta t = 3.1$. For times greater than the selected time limit, $t = 27.1$, the local extrema associated with the initial barotropic vortex pair (Fig. 10a) cease to be global barotropic extrema (e.g., see Fig. 10g).

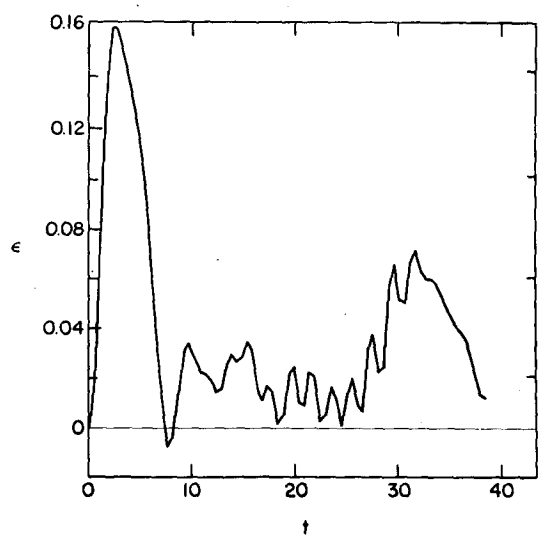

FIG. 12. The time history of the integrated modal energy conversion (4.1) for the numerical solution described in Fig. 10.

the vortex diameter (see Fig. 17c). The modal energy transfer rate ϵ from (4.1) is shown in Fig. 18. It is generally positive for all t in order to supply energy to the barotropic dispersion field, but it does not attain the large values seen in Fig. 12 at small t, which were required for establishing vortex compensation.

A parameter study of the influence of ν is shown in Fig. 19. Most striking in the trajectory plot is the greater temporal uniformity of propagation for the solutions with ν not too small. The westward arrest discussed in Section 4 does not occur except for $\nu = 0$. The velocities at intermediate times ($t \approx 10$) are similar for the $\nu = 0.4$ and 1.0 solutions; they are also similar to the $\nu = 0$ velocity for times well past the propagation arrest (see Fig. 13a). Table 1 presents velocities calculated from the trajectories for each of these three cases. There is a moderate tendency for faster, more southward and less westward propagation as ν increases. On the other hand, these characteristics strongly distinguish these two-mode vortices from the single-mode baroclinic vortex (see Fig. 13a) or the single-mode barotropic vortex (see Figs. 2b and 3a). The speeds in Table 1 correspond to ~4 cm s^{-1} for the dimensional values (2.8). This speed is ~40% faster than the analogous single-mode velocity for $\hat{Q} = 10$ and $\gamma^2 = 2$. The increment is due to the modal coupling implied cooperatively propagating baroclinic and barotropic vortices, as expressed in the moment equations (2.6). For $\nu = 0$, the primary effects were from a barotropic positive center northwest from the baroclinic center and a barotropic negative center in the southeast, both of which contributed a westward and southward tendency to propagation (see Figs. 10e–10h and 11a). The tendency with ν for more southward and less westward propagation (Table 1) is associated with the barotropic positive center moving closer to the baroclinic center and the barotropic negative center moving counterclockwise to a relative position in the east-northeast. There is thus a moderate dependence of the vortex propagation velocity at large times on the initial conditions of the barotropic component, which manifests itself in rather small shifts in the barotropic center locations near the main baroclinic expression of the vortex.

The amplitude decay rates (Fig. 19b) are monotonically decreasing with ν for $t \lesssim 8$. This is consistent with a decreasing modal energy transfer rate ϵ associated with an increasing barotropic com-

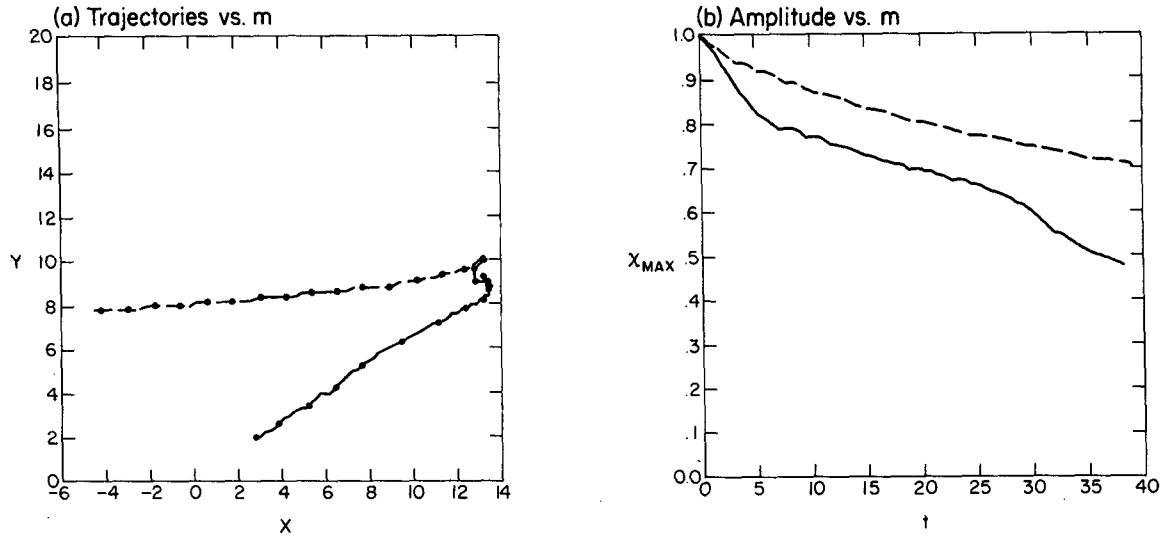

FIG. 13. Trajectory (a) and baroclinic amplitude (b) plots for the one- and two-mode baroclinic vortex numerical solutions (labeled by dashed and solid lines, respectively; see Figs. 1 and 10). In (a), the small squares demark time intervals of $\Delta t = 2.6$.

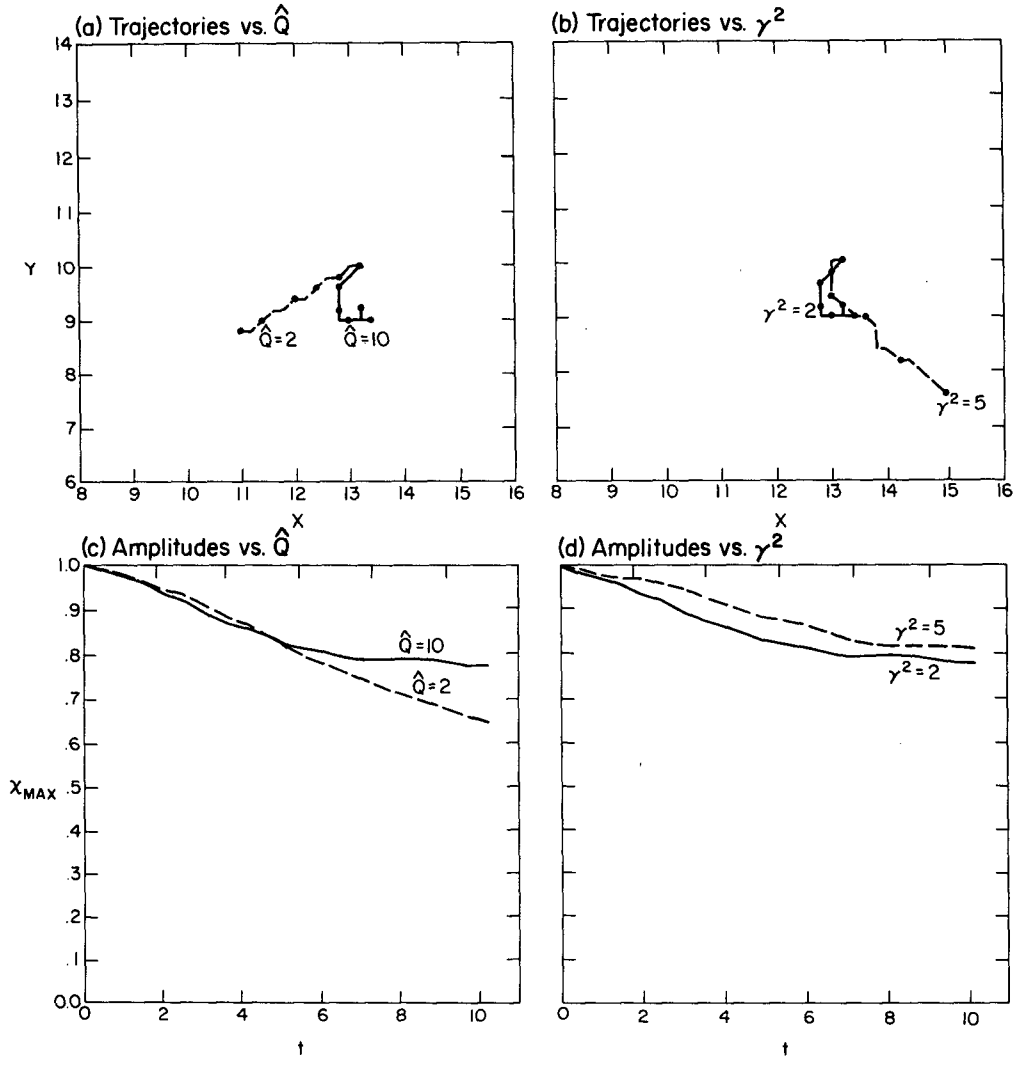

FIG. 14. Trajectory and amplitude plots for variations in the parameters $\hat{Q}$ and γ. Parameters other than the one being varied have the values described in the caption of Fig. 10. The time period shown is $t \in [0, 10.2]$, and the marks on the trajectories correspond to $\Delta t = 2.1$.

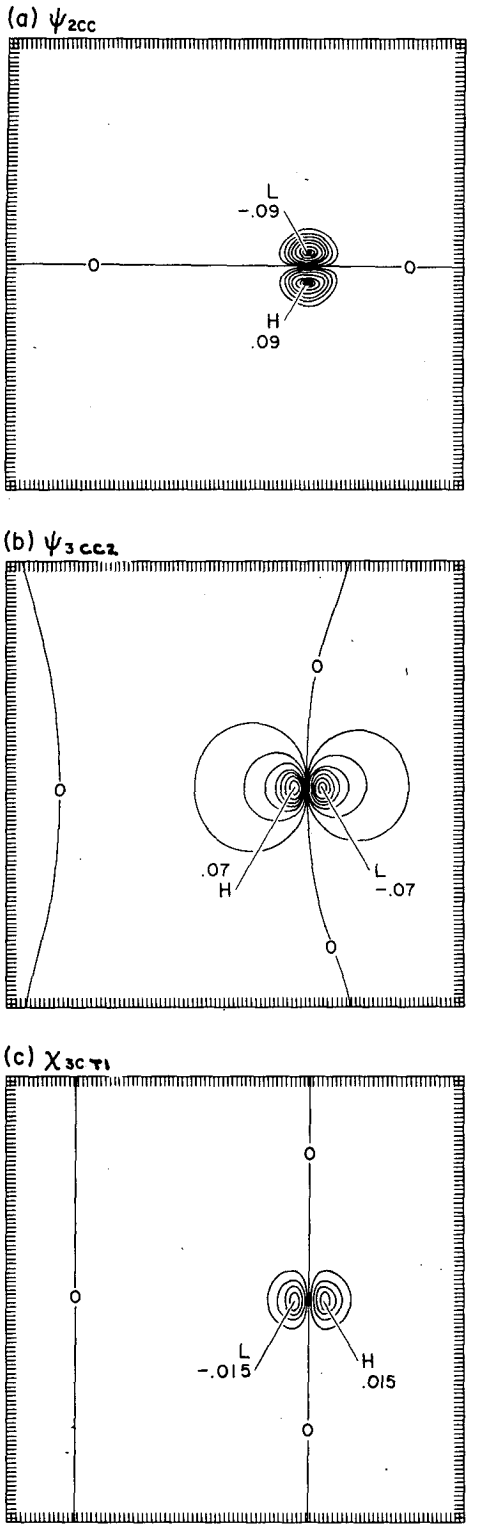

FIG. 15. Spatial coefficients for the small time expansion of Appendix D. Parameters for this calculation are those of Fig. 10. Contour intervals are 0.01 for panels (a) and (b) and 0.003 for panel (c).

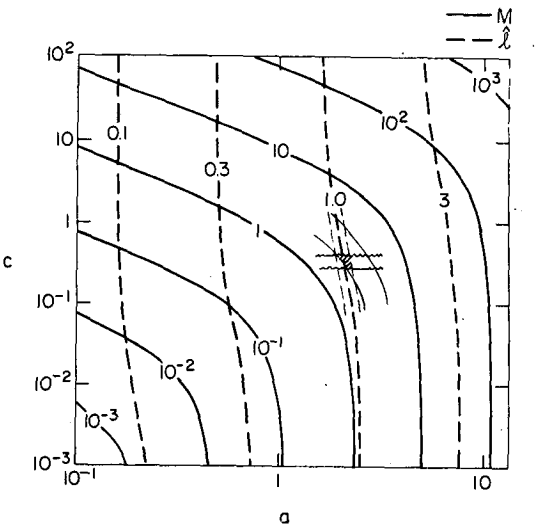

FIG. 16. Barotropic property relations for vortical modons (from Flierl *et al.*, 1978, Fig. 13). a is the modon radius, C its propagation speed, M its streamfunction amplitude, and $\hat{l}$ is half the separation between extrema. Also shown (with thin lines) are the property ranges (4.5) and (with slanted lines) their common area of intersection.

ponent. For intermediate times ($t \in [8,14]$), the $\nu \neq 0$ decay rates become similar to each other and greater than the $\nu = 0$ rate. At even longer times ($t \gtrsim 27$) the $\nu = 0$ rate further increases to a value closer to the intermediate time $\nu \neq 0$ rates (see Fig. 13b). Thus at large times the decay rate appears independent of the initial value.

The various tendencies which can be identified in a $t \to 0$ asymptotic analysis become quite numerous for a mixed-mode vortex. The tendencies shown previously (Figs. 5 and 15) for single-mode and baroclinic, two-mode vortices are relevant in the more general case as well; the tendencies through $O(t^2)$ are unaltered, while those at $O(t^3)$ are quantitatively but not qualitatively altered. There are, however, additional important terms in the mixed-mode case (see Appendix D, Table D3 in particular), the more important of which are shown in Fig. 20. We have seen that isolated concentric maxima in the two modes tend to move together and generally persist in their structures. Thus, parallel tendencies can generally be identified in the two modes. However, they cannot be identical because the spatial operators, which must be inverted to obtain the tendencies, are different (Helmholtz and Poisson). This can be seen most clearly in Fig. 20a, which shows the β-induced tendency for westward propagation and dispersion in the barotropic mode $\psi_{1\beta}$. It is similar in symmetry and amplitude to its baroclinic counterpart ($\chi_{1\beta}$ in Fig. 5b) but of much

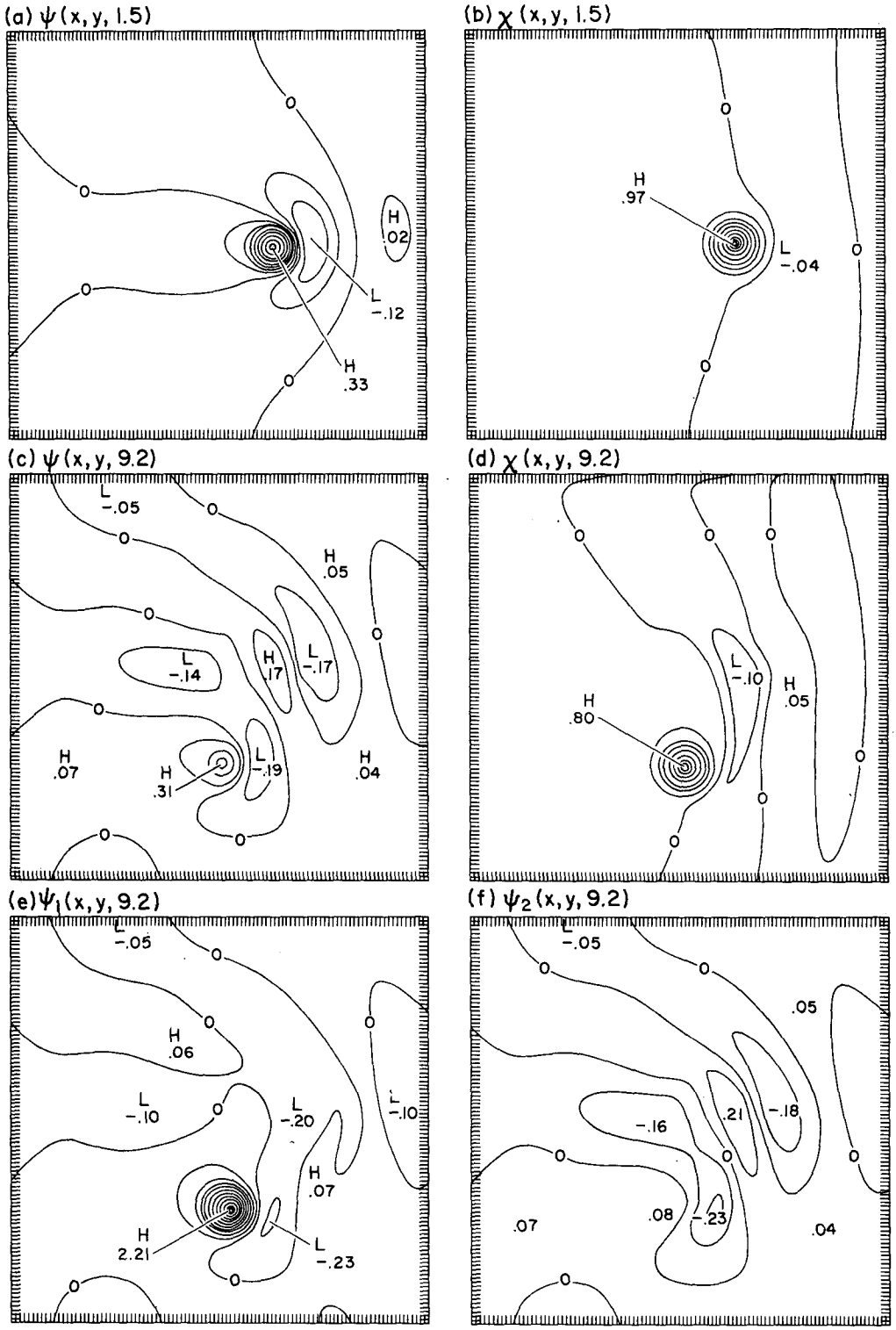

FIG. 17. Barotropic and baroclinic streamfunction patterns are shown in panels (a)–(d) at $t = 1.5$ and 9.5 from a numerical solution for the parameters (3.1) plus $\nu = \delta^{1/2}$, $m = 2$ and $\delta = 0.16$. In addition, panels (e) and (f) show the layer streamfunctions ψ_1 and ψ_2 at $t = 9.2$ by use of Eq. (2.1). The contour interval is 0.1 for all plots except (a), where it is 0.04, and (e), where it is 0.2.

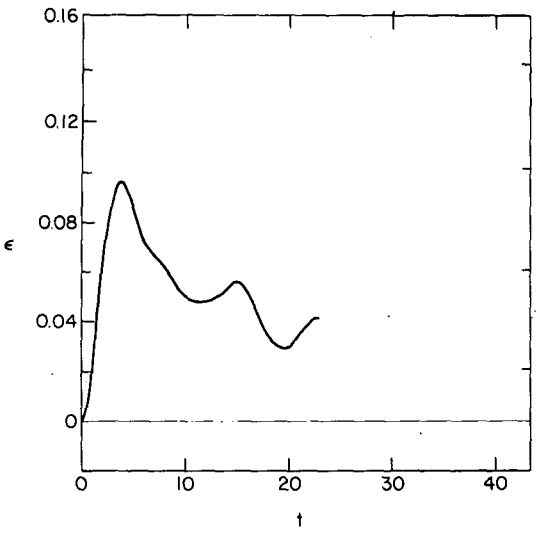

FIG. 18. ϵ from (4.1) for the numerical solution described in Fig. 17.

larger scale. If the linear tendency were dominant, the two modal maxima would not long evolve coherently. Nonlinear modal coupling terms at $O(t^2)$, ψ_{2TT} and χ_{2CT}, are shown in Figs. 20bc. These are meridionally asymmetric patterns which are similar to the previously shown ψ_{2CC} and χ_{2CC} (Figs. 15a and 15e). In the latter case we identified the pattern with southward propagation and in the former with the spinup of a vortex pair. Now that there is an initial axisymmetric barotropic vortex present, all four of these patterns can be identified with nonlinearly induced southward propagation of the main vortices. Similarly, at $O(t^3)$ the nonlinear terms produce a westward propagation tendency (Figs. 20de). As indicated in the legends, these $O(t^3)$ terms are composites of several terms acting similarly. Previous manifestations of zonal propagation were shown in Figs. 5f, 15b and 15c. When the additional modal coupling terms are added as in Figs. 20d and 20e, all tendencies are westward; the propagation arrest which arises from $\chi_{3C\,T1}$ is not dominant.

There is a longer term tendency for these mixed-mode solutions to approach a compensated state, as was briefly discussed above. This appears to be a general tendency when $\hat{Q}$ and γ^2 are large and δ is small. Fig. 21 shows the ratio of modal vortex amplitudes as a function of time for different initial vertical structures (different ν). In each case the solutions vary only moderately about the compensation ratio $\delta^{1/2}$ after an initial period of adjustment. Two other cases, whose solutions were partly described in Fig. 14 but whose amplitude ratios are not shown in Fig. 21, also approach a compensated state. Their parameters were $\{\hat{Q},\gamma^2,\nu\} = \{10,5,0\}$ and $\{2,2,0\}$ in addition to standard values for the other ones. A further case (also not plotted) was done with $\{\hat{Q},\gamma^2,\nu\} = \{10,\ 2,\ -0.4\}$. Its vortex also went through an initial period of eastward, modon-like propagation and eventually reached compensation, but the time required for this evolu-

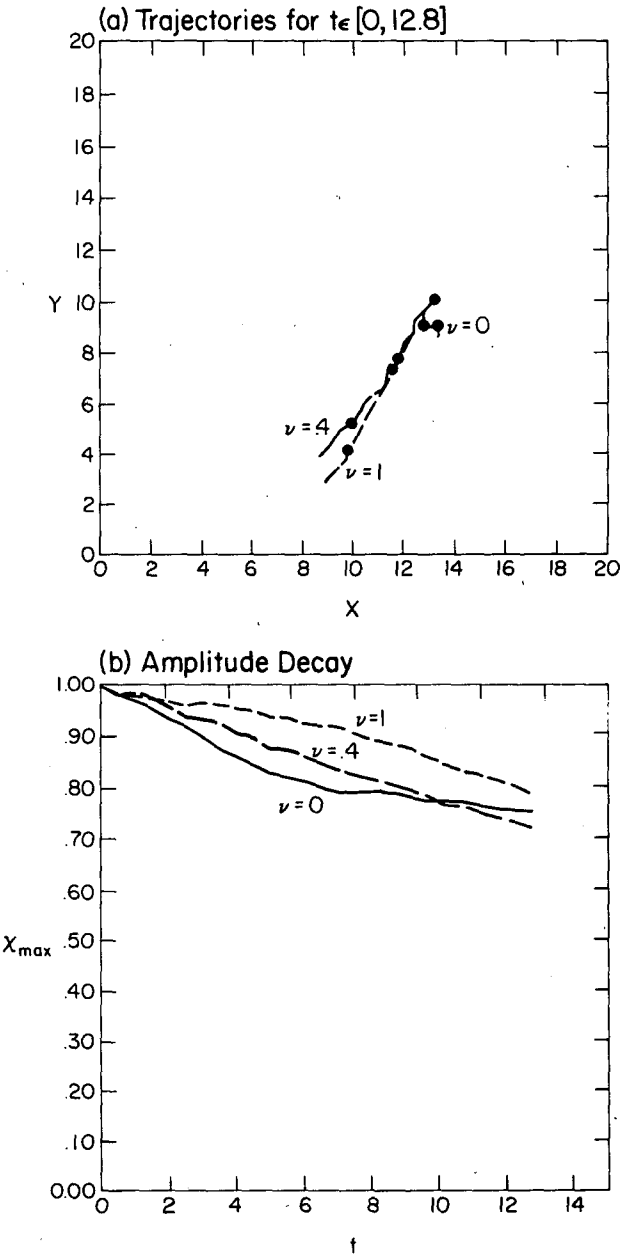

FIG. 19. Trajectory (a) and amplitude (b) plots for the baroclinic component of mixed mode vortex numerical solutions which differ only in their initial barotropic amplitude ν. Three values of ν are shown, two of which are the solutions of Figs. 10 and 17. In (a) the marks along the trajectories are separated by $\Delta t = 5.2$.

tion ($\Delta t \approx 45$) was much larger than for the $\nu \geq 0$ cases in Fig. 21.

We can examine both the tendency for the persistence of a vortex in a compensated state and the manner in which compensation is approached. The former issue is best examined in the layer rather than the modal equations. From Eqs. (2.1) and (2.4), we obtain

$$\left.\begin{aligned}&\left\{\left[\nabla^2 - \frac{\gamma^2}{1+\delta}\right]\frac{\partial}{\partial t} + \frac{\partial}{\partial x} + K_*\nabla^6\right\}\psi_1 + QJ(\psi_1,\nabla^2\psi_1) + \frac{\gamma^2}{1+\delta}\frac{\partial}{\partial t}\psi_2 + \frac{Q\gamma^2}{1+\delta}J(\psi_1,\psi_2) = 0\\ &\left\{\left[\nabla^2 - \frac{\delta\gamma^2}{1+\delta}\right]\frac{\partial}{\partial t} + \frac{\partial}{\partial x} + K_*\nabla^6\right\}\psi_2 + QJ(\psi_2,\nabla^2\psi_2) + \frac{\delta\gamma^2}{1+\delta}\frac{\partial}{\partial t}\psi_1 - \frac{\delta\gamma^2}{1+\delta}QJ(\psi_1,\psi_2) = 0\end{aligned}\right\}. \quad (5.1)$$

Compensation occurs for χ order one when

$$\left.\begin{aligned}&\psi_1 = O(\delta^{-1/2}),\\ &\psi_2 = \begin{cases} o(\delta^{1/2}) \text{ in the vicinity of } \chi = \chi_{\max} \\ O(\delta^{1/2}) \text{ elsewhere.}\end{cases}\end{aligned}\right\}. \quad (5.2)$$

We formally expand (5.1) as $\delta \to 0$ under the assumptions that $\hat{Q}$, γ, K_*, and $\mu \equiv Q\gamma^2\delta^{1/2}$ are order 1 and that

$$\left.\begin{aligned}\psi_1 &= \delta^{-1/2}\phi_1 + \ldots\\ \psi_2 &= \delta^{1/2}\phi_2 + \ldots\end{aligned}\right\}. \quad (5.3)$$

The result is

$$\left.\begin{aligned}&\left\{(\nabla^2 - \gamma^2)\frac{\partial}{\partial t} + \frac{\partial}{\partial x} + K_*\nabla^6\right\}\phi_1 + \hat{Q}J(\phi_1,\nabla^2\phi_1) = -\mu J(\phi_1,\phi_2)\\ &\left\{\nabla^2\frac{\partial}{\partial t} + \frac{\partial}{\partial x} + K_*\nabla^6\right\}\phi_2 + \gamma^2\frac{\partial}{\partial t}\phi_1 = \mu\left[J(\phi_1,\phi_2) - \frac{1}{\gamma^2}J(\phi_2,\nabla^2\phi_2)\right]\end{aligned}\right\}, \quad (5.4)$$

plus neglected terms of relative $O(\delta)$. For the standard parameter values [Eq. (3.1) plus $\delta = 0.16$], μ is 3.8, and, for the cases cited above where compensation develops, μ is between 0.8 and 9.5. Thus, μ is not necessarily a small number. However, it is helpful to interpret compensation persistence partially as a consequence of the small μ form of (5.4). In this case, ϕ_1 satisfies the single-mode baroclinic vortex equation studied in Section 3, and ϕ_2 satisfies a weakly damped, nonresonantly forced, linear, barotropic Rossby wave equation. Barotropic Rossby waves are highly dispersive, and it is therefore unlikely that the lower layer streamfunction amplitude will efficiently increase at any point in the fluid while ϕ_1 propagates as a single-mode vortex. For $\mu > 0$, Eqs. (5.4) do not have familiar properties, and they must be integrated numerically. This is done for compensated initial conditions,

$$\phi_1 = e^{-r^2}, \quad \phi_2 = 0, \quad (5.5)$$

which are approximately equivalent to Eq. (2.7) when $\nu = \delta^{1/2}$. The spatial patterns of the resulting ϕ_1 and ϕ_2 are shown in Fig. 22 for three values of μ at $t = 15.3$. In all cases, there are an O(1), southwestward propagating vortex in ϕ_1 and an O(1), wave dispersion field in ϕ_2. In gross measure, then, the compensating nature of Eqs. (5.4) is insensitive to μ. Trajectories for the ϕ_1 vortex are shown in Fig. 23. There is a strong dependence of the propagation rate on μ, but it is the same one discussed above for one- versus two-mode vortices (note the asterisk locations on Fig. 23). Only for the largest value of μ in Figs. 22 and 23 do the uniform propagation rate and approximate axial symmetry of the ϕ_1 vortex become disrupted near the end of the integration period shown. Also, at this time the ϕ_2 pattern begins to show the main vortex, which is a departure from exact compensation. This μ value (12.5) is larger than for any other case discussed in this paper, and since $\mu \propto \delta^{1/2}$ by definition, excessively large μ is inconsistent with a small δ expansion. Global maximum ϕ_2 amplitudes are plotted as a function of time in Fig. 24. These amplitudes are in fact a decreasing function of μ, indicating that intensification of ϕ_2 away from compensation is inhibited by the terms on the right-hand side of (5.4).

Thus, we have a means of interpreting compensation persistence in terms of the dispersion of lower layer Rossby waves forced by the thermocline interfacial deformations of the upper layer vortex.

TABLE 1. Two-mode vortex propagation speeds as a function of ν.†

ν	Time interval	$\dot{x}_c$	$\dot{y}_c$	$\lvert\dot{\mathbf{x}}_c\rvert$	$\tan^{-1}(\dot{y}_c/\dot{x}_c)$*
0	[30.2,38.4]	−0.51	−0.32	0.60	238
0.4	[5.6,13.8]	−0.42	−0.46	0.62	222
1.0	[5.6,13.8]	−0.39	−0.56	0.68	215

* Angles in degrees measured clockwise from north.

† The $m = 1$ propagation speeds can be calculated from Fig. 3a. The comparison values for the final four columns of this table are −0.49, −0.13, 0.51 and 256, respectively.

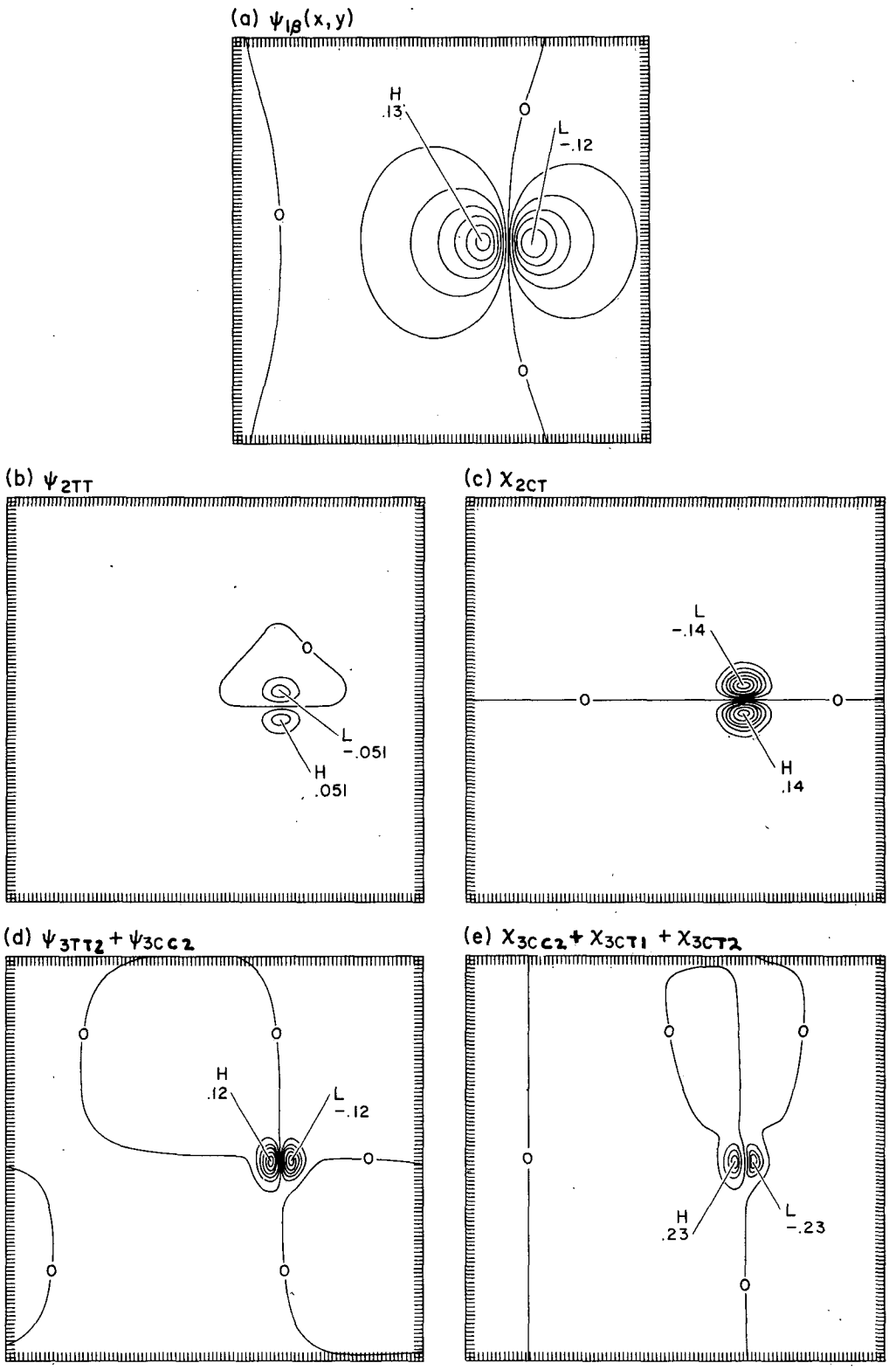

FIG. 20. Selected spatial coefficients of powers of t in a small time expansion for an initially compensated vortex (the parameters are those of Fig. 17). The contour interval is 0.02 except in (e) where it is 0.06.

The approximate dynamical separation of the two layers is a consequence of a thin upper layer and the amplitude ordering of (5.2).

Other processes can occur when the streamfunction orders are not as indicated in (5.2). In Section 4 it was shown that for an initial *deficit* of a barotropic component—or an initial vortex component in ϕ_2 of opposite phase to the ϕ_1 vortex—a baroclinic vortex will spin up a barotropic vortex pair. When the barotropic amplitude is approximately large enough to be compensating, the baroclinic vortex center will shift over the barotropic positive center by the vortical modon instability mechanism. For an initial *excess* of a barotropic component, it appears that barotropic wave dispersion will efficiently erode the barotropic vortex component until its amplitude is approximately compensating. Fig. 9a shows that a barotropic single-mode vortex does have a rapid amplitude decay due to wave dispersion (*n.b.*, there is no modal coupling and the frictional decay rate is weak). For the two-mode vortex solution with $\nu = 1$ (see Figs. 19 and 21), the barotropic vortex amplitude decreases by 70% in the first 9 time units, while the modal transfer rate ϵ from (4.1) remains small and generally positive. The barotropic decay toward compensation, therefore, is not due to nonlinear transfer to the baroclinic mode vortex nor to the weak friction; thus, it must be a wave dispersion process. Note that both directions of approach to compensation depend on the baroclinic component being sufficiently strong (or Q sufficiently large, since Q is defined from the baroclinic scales in Section 2). Only through the nonlinear terms is there any modal coupling.

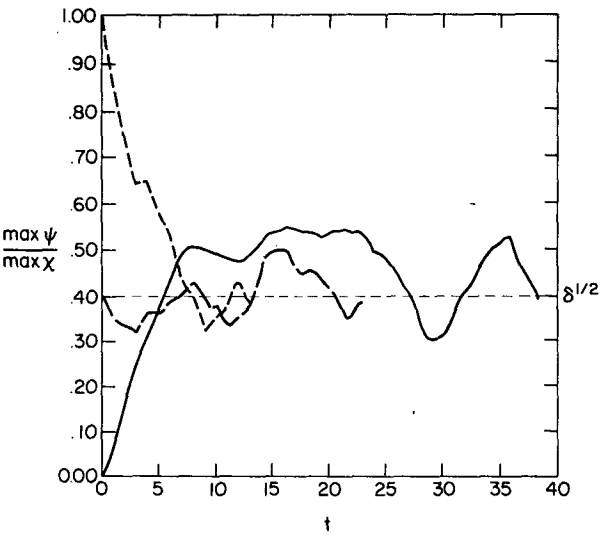

FIG. 21. Time histories of the ratio of barotropic and baroclinic maxima for mixed mode vortices (the latter maximum is global and the former is a local one in the vicinity of the baroclinic maximum). The three curves are for the numerical solutions shown in Fig. 19. The value $\delta^{1/2}$ corresponds to perfect compensation.

6. Summary and comparison with other solutions

We have examined various numerical solutions for the evolution of an isolated, axisymmetric vortex for different values of parameters representing the vortex size and strength (γ and Q), the fractional depth of the ocean thermocline (δ), the rate of frictional decay ($K*$), the degree of vertical modal coupling (m), and the initial fractional barotropic component (ν). A number of interesting phenomena have been found which are due to the vortex amplitude being large enough for the nonlinear advective processes to be important. For sufficiently large Q and γ, the rate of vortex decay can become small enough to be significantly influenced by even weak frictional processes, even though there are also significant losses to both barotropic and baroclinic wave dispersion. The baroclinic vortex propagation rate can have a large meridional component due to both baroclinic nonlinear self-interactions and baroclinic-barotropic modal coupling; the westward linear propagation tendency due to β is enhanced by the former process and can either be enhanced or opposed by the latter, depending on initial conditions. For large Q and γ and small δ, there is a general tendency for any vortex with a significant initial baroclinic component to approach a state of deep compensation, with little lower layer expression of the main vortex, but also with an energetic field of barotropic eddies outside the main vortex.

The solutions obtained are for circumstances too simple to warrant detailed comparisons with observed rings. However, we would predict certain tendencies to occur. Because the Gulf Stream generates high- and low-pressure rings, respectively, to its north and south, there should be a tendency for these rings to return to the Stream due to the nonlinear meridional propagation tendency described above. The westward propagation velocities of rings should, on the whole, be faster than linear velocities. The ring decay rate should be strongly influenced by even weak nonconservative processes [thus, in retrospect, the study of Schmitz and Vastano (1975) can be considered even more relevant after our examination of many of the processes they neglected]. Finally, rings can be viewed as a probably significant source of other types of eddy energy in the ocean, not primarily through the mechanism of baroclinic wave dispersion [as discussed by Flierl (1977)] but more strongly through nonlinear transfers to the more dispersive barotropic mode (*n.b.*, ϵ is universally positive in Figs. 12 and 18). The most relevant new observa-

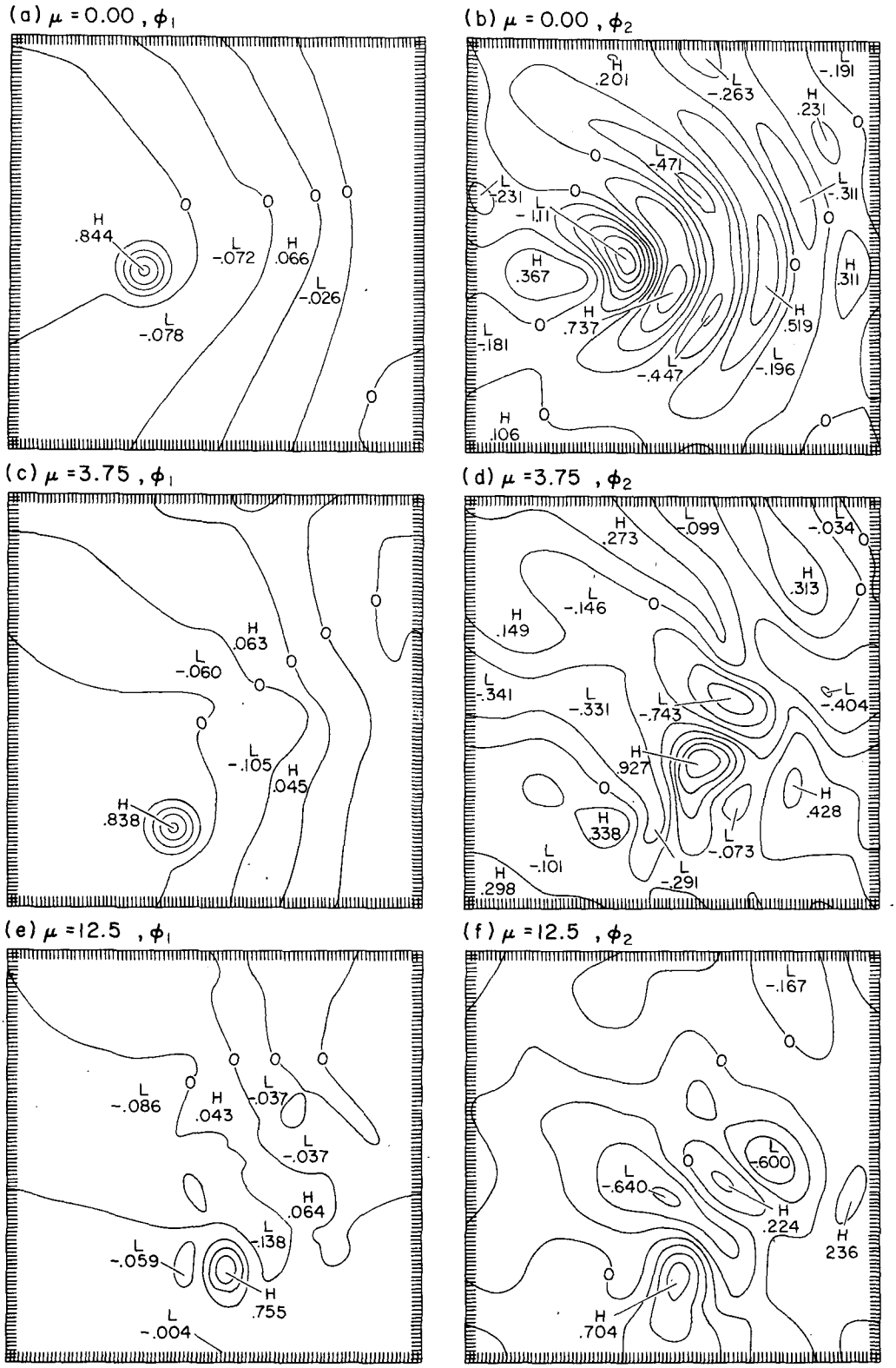

FIG. 22. Renormalized layer streamfunctions ϕ_1 and ϕ_2 which are solutions of the small δ equations (5.4) with initial conditions (5.5). The patterns are at $t = 15.3$ for three values of μ. The contour interval is 0.2.

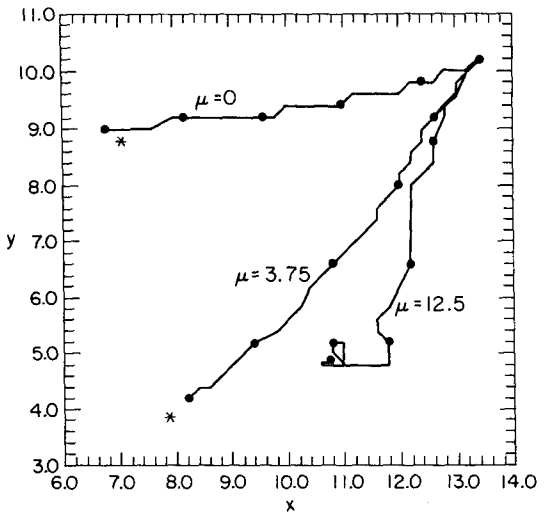

FIG. 23. Trajectories of the position of the maximum value of ϕ_1 for $t \in [0,15.3]$ and three values of μ. Also marked with asterisks are the positions of χ_{max} at $t = 15.3$ from the full equations (2.4) with parameter values similar to those for the two solutions of (5.4) with the smaller μ values (i.e., comparable to $\mu = 0$ is the $m = 1$ solution shown in Fig. 2 and comparable to $\mu = 3.75$ is the $\{\nu = 0.4, m = 2\}$ solution shown in Fig. 17). The dots demark time intervals of 3.1.

tion which we would recommend is the spatial distribution of deep currents in the vicinity of a ring.

Bretherton and Karweit (1975) presented one solution for an initially compensated, low-pressure vortex from a model similar to ours but with higher vertical resolution (six layers). We estimate their parameter values as $\gamma^2 = 1.8, \hat{Q} = 2.8, \delta \approx 0.16$ and $K*$ small. They showed three upper layer streamfunction patterns (Figs. 10, 11 and 12 for $t \approx 0$, 8 and 22, respectively). Their eddy decreased in amplitude and propagated to the west-northwest. The fractional amplitude decay (13%) and propagation velocities ($\dot{x}_c \approx -0.6$ and $\dot{y}_c \approx 0.4$) during the first interval are quite consistent with those of our solutions, while those during the second interval (50%, −0.7 and 0.5, respectively) are all excessive compared to our solutions. It seems likely that edge effects in their solutions, due to their relatively smaller horizontal domain, account for these differences at later times.

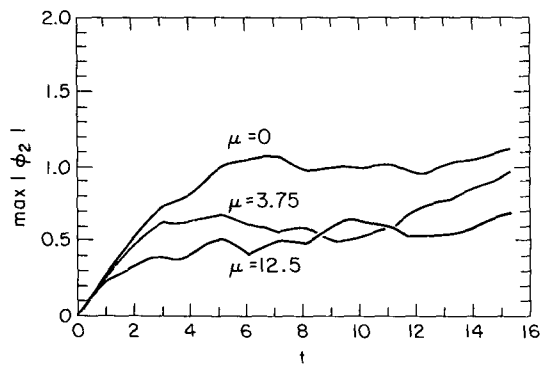

FIG. 24. Maximum values of $|\phi_2|$ versus time for the μ values of 0, 3.75 and 12.5.

Mied's (1978) study (carried out simultaneously with ours) of the evolution of a Gaussian eddy in a two-layer primitive model also gives similar results to ours. He considers vortices of fixed size ($\gamma^2 = 2.3$) and nearly fixed baroclinic velocity ($Q = 0.5$ to 0.8 with $\delta = 0.25$) and variable barotropic velocity ($\nu = 1.1$ to 15). When ν is not large, the motion becomes compensated. For the large ν cases, though, the evolution is similar to a barotropic eddy case with rapid dispersion and essentially similar motions in both layers.

Acknowledgments. The authors greatly appreciate the programming assistance of Mrs. Julianna Chow and the typing of Ms. H. Howard. One of the authors (JM) was supported by the National Science Foundation through its grant to NCAR, while the other (GF) was partly supported in the same way as a summer visitor to NCAR and partly supported through a grant from the National Science Foundation (76-80060-OCE) to MIT.

APPENDIX A

Numerical Techniques and Cases

The numerical solution presented in this paper is based on a finite-difference representation of (2.4) in a periodic domain of dimension L. The finite-difference formulas were centered second-order ones in both space and time; in particular, the nonlinear Jacobian operations were calculated by the spatially conservative formula of Arakawa (1966).

TABLE A1. Numerical cases.

m	$\hat{Q}$	γ^2	$K*$	ν	δ	Section(s) where discussed
1	10	2	5×10^{-4}	—	—	3
1	0	2	5×10^{-4}	—	—	3
1	0.5	2	5×10^{-4}	—	—	3
1	2	2	5×10^{-4}	—	—	3
1	10	0	5×10^{-4}	—	—	3
1	10	1	5×10^{-4}	—	—	3
1	10	5	5×10^{-4}	—	—	3
1	10	2	5×10^{-5}	—	—	3
2	10	2	5×10^{-4}	0	0.16	4, 5
2	2	2	5×10^{-4}	0	0.16	4, 5
2	10	5	5×10^{-4}	0	0.16	4, 5
2	10	2	5×10^{-4}	0.4	0.16	5
2	10	2	5×10^{-4}	1	0.16	5
2	10	2	5×10^{-4}	−0.4	0.16	5

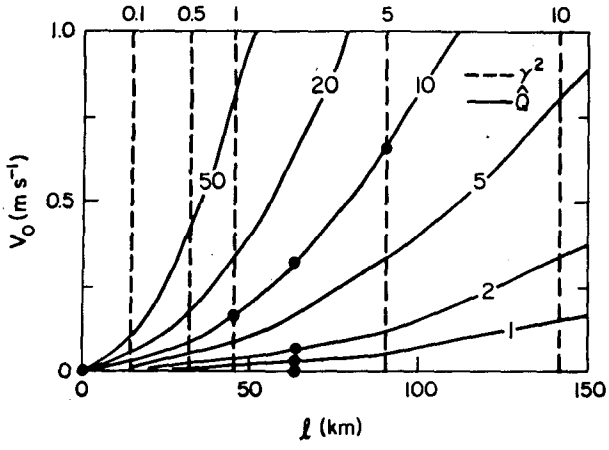

FIG. A1. Contours of $\hat{Q}$ (solid lines) and γ^2 (dashed lines), as defined in Eq. (2.5), as a function of V_0, a typical particle speed [see the footnote to Eq. (2.8) for an interpretation of V_0] and l, a pressure e-folding radius. β, R and δ are as in Eqs. (2.8) and (2.9). Also plotted (as dots) are the $\hat{Q}$, γ^2 values for the numerical cases listed in Table A1.

The numerical parameters of the calculations were

$$\left.\begin{aligned} L &= 20.0 \\ x_0 &= 16.7 \\ y_0 &= 10.0 \\ \Delta x &= \Delta y = 0.2 \\ \Delta t &= 0.014 \end{aligned}\right\}, \tag{A1}$$

where (x_0,y_0) is the initial vortex center [see Eq. (2.7)], Δx and Δy are the spatial resolution scales, and Δt is the temporal resolution scale. Dividing the resolution scales by 2 yielded numerical solutions which were unimportantly different from the ones calculated from (A1).

A listing of the parameters for the numerical solution cases, including a reference to the sections where they are discussed, is given in Table A1, and a plot of the $\hat{Q}$ and γ values used, as a function of V_0 and l, is given in Fig. A1.

APPENDIX B

Linear, Inviscid Vortex Evolution

Following Flierl (1977), we can write the solution to Eqs. (2.4b) and (2.7), in an infinite domain with $x_0 = y_0 = \hat{Q} = Q = K_* = 0$, as

$$\chi(x,y,t) = \frac{1}{2}\int_0^\infty ds\, s e^{-s^2/4} \times J_0\left\{s\left[\left(x + \frac{t}{s^2+\gamma^2}\right)^2 + y^2\right]^{1/2}\right\}. \tag{B1}$$

If we define the zonal propagation velocity $V(t)$ as the zonal translation speed of the location of the maximum value in χ, then

$$V(0) = -\frac{1}{4} + \gamma^2 \frac{e^{\gamma^2/4}}{16} E_1(\gamma^2/4), \tag{B2}$$

where $E_1(z) = \int_z^\infty e^{-t}dt/t$ is an exponential integral. For $\gamma^2 = 2$—the standard parameter value in (3.1)—we evaluate (B2) to give $V(0) = -0.135$. As $t \to \infty$, $V(t) \to -1/\gamma^2 = -0.5$.

If we define $\chi_{\max}(t)$ as the spatial maximum value of χ at time t, then

$$\chi_{\max}(t) = 1 - \frac{1}{2}\int_0^t d\tau \int_0^\infty ds \frac{s^2 ds}{s^2+\gamma^2} \times e^{-s^2/4} J_1\left\{s\tau\left[V(\tau) + \frac{1}{s^2+\gamma^2}\right]\right\} = 1 - t^2/T^2 + O(t^3), \tag{B3}$$

where

$$T = \frac{1}{4}\int_0^\infty \frac{s^2 ds}{s^2+\gamma^2} e^{-s^2/4}\left[V(0) + \frac{1}{s^2+\gamma^2}\right]. \tag{B4}$$

For $\gamma^2 = 2$, $T = 12.0$.

APPENDIX C

Frictional Vortex Evolution

Eqs. (2.4a) and (2.4b) would apply to motions in a uniformly rotating environment (i.e., $\beta = 0$) if the terms $\partial\psi/\partial x$ and $\partial\chi/\partial x$ were deleted. For an initially Gaussian vortex, Eq. (2.7)—the baroclinic streamfunction solution for all time, in an infinite domain—can be written as

$$\chi(x,y,t) = \frac{1}{2}\int_0^\infty ds\, s \exp\left(-s^2/4 - K_* t \frac{s^6}{s^2+\gamma^2}\right) \times J_0\{s(x^2+y^2)^{1/2}\}, \tag{C1}$$

where at $t = 0$, χ is centered at the origin. Note that this solution is independent of nonlinearity and barotropic modal coupling and that it is non-propagating.

APPENDIX D

A Small Time Expansion

The solution to (2.4) and (2.7) can be represented as a Taylor series in powers of the time. We define

$$\left.\begin{aligned} \psi &= \nu e^{-r^2} + \sum_{n=1}^{\infty} \psi_n t^n \\ \chi &= e^{-r^2} + \sum_{n=1}^{\infty} \chi_n t^n \end{aligned}\right\}, \tag{D1}$$

where the coefficients for $n = 1$, 2 and 3 are each defined as a sum of several terms. These terms have subscripts which identify their order and the process which gives rise to them (e.g., β = the β-effect, K = friction, CC = baroclinic-baroclinic nonlinear interaction):

$$\psi_1 = [m-1](\psi_{1\beta} + \psi_{1K})$$

$$\nabla^2\psi_{1\beta} = -\nu \frac{\partial}{\partial x} e^{-r^2} \tag{D2}$$

$$\nabla^2\psi_{1K} = -\nu K_* \nabla^6 e^{-r^2}$$

$$\chi_1 = (\chi_{1\beta} + \chi_{1K})$$

$$(\nabla^2 - \gamma^2)\chi_{1\beta} = -\frac{\partial}{\partial x} e^{-r^2} \tag{D3}$$

$$(\nabla^2 - \gamma^2)\chi_{1K} = -K_* \nabla^6 e^{-r^2}$$

$$\psi_2 = [m-1](\psi_{2\beta} + \psi_{2K} + \psi_{2CC} + \psi_{2TT})$$

$$\nabla^2\psi_{2\beta} = -\frac{1}{2}\frac{\partial}{\partial x}\psi_1$$

$$\nabla^2\psi_{2K} = -\frac{1}{2} K_* \nabla^6 \psi_1 \tag{D4}$$

$$\nabla^2\psi_{2CC} = -\frac{Q}{2}[J(e^{-r^2}, \nabla^2\chi_1) + J(\chi_1, \nabla^2 e^{-r^2})]$$

$$\nabla^2\psi_{2TT} = -\frac{Q\nu}{2}[J(e^{-r^2}, \nabla^2\psi_1) + J(\psi_1, \nabla^2 e^{-r^2})]$$

$$\chi_2 = (\chi_{2\beta} + \chi_{2K} + \chi_{2CC} + \chi_{2CT})$$

$$(\nabla^2 - \gamma^2)\chi_{2\beta} = -\frac{1}{2}\frac{\partial}{\partial x}\chi_1$$

$$(\nabla^2 - \gamma^2)\chi_{2K} = -\frac{1}{2} K_* \nabla^6 \chi_1$$

$$(\nabla^2 - \gamma^2)\chi_{2CC} = -\frac{\hat{Q}}{2}[J(e^{-r^2}, \nabla^2\chi_1) + J(\chi_1, \nabla^2 e^{-r^2})] \tag{D5}$$

$$(\nabla^2 - \gamma^2)\chi_{2CT} = -\frac{Q}{2}[m-1][J(\psi_1, \nabla^2 e^{-r^2}) + J(e^{-r^2}, \nabla^2\psi_1) - \gamma^2 J(\psi_1, e^{-r^2}) - \nu\gamma^2 J(e^{-r^2}, \chi_1)]$$

$$\psi_3 = [m-1](\psi_{3\beta} + \psi_{3K} + \psi_{3T\,T1} + \psi_{3T\,T2} + \psi_{3C\,C1} + \psi_{3C\,C2})$$

$$\nabla^2\psi_{3\beta} = -\frac{1}{3}\frac{\partial}{\partial x}\psi_2$$

$$\nabla^2\psi_{3K} = -\frac{K_*}{3}\nabla^6\psi_2$$

$$\nabla^2\psi_{3T\,T1} = -\frac{Q}{3} J(\psi_1, \nabla^2\psi_1) \tag{D6}$$

$$\nabla^2\psi_{3T\,T2} = -\nu\frac{Q}{3}[J(e^{-r^2}, \nabla^2\psi_2) + J(\psi_2, \nabla^2 e^{-r^2})]$$

$$\nabla^2\psi_{3C\,C1} = -\frac{Q}{3} J(\chi_1, \nabla^2\chi_1)$$

$$\nabla^2\psi_{3C\,C2} = -\frac{Q}{3}[J(e^{-r^2}, \nabla^2\chi_2) + J(\chi_2, \nabla^2 e^{-r^2})]$$

$$\chi_3 = (\chi_{3\beta} + \chi_{3K} + \chi_{3C\,C1} + \chi_{3C\,C2} + \chi_{3C\,T1} + \chi_{3C\,T2} + \chi_{3C\,T3})$$

$$(\nabla^2 - \gamma^2)\chi_{3\beta} = -\frac{1}{3}\frac{\partial}{\partial x}\chi_2$$

$$(\nabla^2 - \gamma^2)\chi_{3K} = -\frac{K_*}{3}\nabla^2\chi_2$$

$$(\nabla^2 - \gamma^2)\chi_{3C\,C1} = -\frac{\hat{Q}}{3} J(\chi_1, \nabla^2\chi_1)$$

$$(\nabla^2 - \gamma^2)\chi_{3C\,C2} = -\frac{\hat{Q}}{3}[J(\chi_2, \nabla^2 e^{-r^2}) + J(e^{-r^2}, \nabla^2\chi_2)] \tag{D7}$$

$$(\nabla^2 - \gamma^2)\chi_{3C\,T1} = -\frac{Q}{3}[m-1][J(\psi_2, \nabla^2 e^{-r^2}) + J(e^{-r^2}, (\nabla^2 + \gamma^2)\psi_2)]$$

$$(\nabla^2 - \gamma^2)\chi_{3C\,T2} = -\frac{Q}{3}[m-1][\nu J(e^{-r^2}, (\nabla^2 - \gamma^2)\chi_2) + \nu J(\chi_2, \nabla^2 e^{-r^2})]$$

$$(\nabla^2 - \gamma^2)\chi_{3C\,T3} = -\frac{Q}{3}[m-1][J(\psi_1, (\nabla^2 - \gamma^2)\chi_1) + J(\chi_1, \nabla^2\psi_1)].$$

In Sections 3–5 a sequence of three different problems are considered:

a. Section 3: $m = 1$, $\nu = 0$

In this case $\psi_n \equiv 0$ for all n. Only the following coefficients are nonzero: $\chi_{1\beta}$, χ_{1K}, $\chi_{2\beta}$, χ_{2K}, χ_{2CC}, $\chi_{3\beta}$, χ_{3K}, $\chi_{3C\,C1}$, $\chi_{3C\,C2}$. For the standard parameter values (3.1), the peak amplitudes for each of these

TABLE D1. Peak amplitudes for coefficients in a small time expansion for a single-mode vortex.*

Coefficient	Peak amplitude
$\chi_{1\beta}$	0.14
χ_{1K}	0.012
$\chi_{2\beta}$	0.024
χ_{2K}	0.0009
χ_{2CC}	0.14
$\chi_{3\beta}$	0.006
χ_{3K}	0.003
$\chi_{3C\,C1}$	0.014
$\chi_{3C\,C2}$	0.12

* These calculations are based on the standard parameters (3.1).

TABLE D2. Peak amplitudes for coefficients in a small time expansion for a two-mode, initially baroclinic vortex.*

Coefficient	Peak amplitude
$\chi_{1\beta}$	0.14**
χ_{1K}	0.012**
ψ_{2CC}	0.088
$\chi_{2\beta}$	0.024**
χ_{2K}	0.0009**
χ_{2CC}	0.14**
$\psi_{3\beta}$	0.004
ψ_{3K}	0.002
$\psi_{3C\,C1}$	0.009
$\psi_{3C\,C2}$	0.07
$\chi_{3\beta}$	0.006**
χ_{3K}	0.003**
$\chi_{3C\,C1}$	0.014**
$\chi_{3C\,C2}$	0.12**
$\chi_{3C\,T1}$	0.015

* These calculations are based upon the standard parameters (3.1) plus $m = 2$ and $\nu = 0$.
** Identical to corresponding coefficient in Table D1.

coefficients are listed in Table D1. A subset of these coefficients is plotted in Fig. 5.

b. *Section 4: $m = 2$, $\nu = 0$*

In this case $\psi_0 = \psi_1 = 0$ but ψ_2 and ψ_3 are nonzero. Only the following coefficients in (D2)–(D7) are nonzero: $\chi_{1\beta}, \chi_{1K}, \psi_{2CC}, \chi_{2\beta}, \chi_{2K}, \chi_{2CC}, \psi_{3\beta}, \psi_{3K}, \psi_{3C\,C1}, \psi_{3C\,C2}, \chi_{3\beta}, \chi_{3K}, \chi_{3C\,C1}, \chi_{3C\,C2}, \chi_{3C\,T1}$. For the standard parameter values (3.1) plus $\delta = 0.16$ ($Q = 4.76$), the peak amplitudes for each of these coefficients are listed in Table D2 and a subset is plotted in Fig. 15.

TABLE D3. Peak amplitudes for coefficients in a small time expansion for a two-mode compensated vortex.*

Coefficient	Peak amplitude
$\psi_{1\beta}$	0.13
ψ_{1K}	0.006
$\chi_{1\beta}$	0.14**
χ_{1K}	0.012**
$\psi_{2\beta}$	0.10
ψ_{2K}	0.0005
ψ_{2CC}	0.088†
ψ_{2TT}	0.051
$\chi_{2\beta}$	0.024**
χ_{2K}	0.0009**
χ_{2CC}	0.14**
χ_{2CT}	0.135
$\psi_{3\beta}$	0.05
ψ_{3K}	0.003
$\psi_{3T\,T1}$	0.005
$\psi_{3T\,T2}$	0.018
$\psi_{3C\,C1}$	0.009†
$\psi_{3C\,C2}$	0.09
$\chi_{3\beta}$	0.010
χ_{3K}	0.005
$\chi_{3C\,C1}$	0.014
$\chi_{3C\,C2}$	0.16
$\chi_{3C\,T1}$	0.028
$\chi_{3C\,T2}$	0.076
$\chi_{3C\,T3}$	0.007

* These calculations are based upon the standard parameters (3.1) plus $m = 2$ and $\nu = 0.4$.
** Identical to corresponding coefficients in Tables D1 and D2.
† Identical to corresponding coefficients in Table D2.

c. *Section 5: $m = 2$, $\nu \neq 0$*

In this case all coefficients in (D1)–(D7) are nonzero. For the standard parameter values (3.1) plus $\delta = 0.16$ ($Q = 4.76$) and $\nu = 0.4$, the peak amplitudes for each of these coefficients are listed in Table D3 and a subset is plotted in Fig. 20.

REFERENCES

Arakawa, A., 1966: Computational design for long term numerical integration of the equations of fluid motion: Two-dimensional incompressible flow. Part I. *J. Comput. Phys.*, **1**, 119–143.

Bretherton, F., and M. Karweit, 1975: Mid-ocean, mesoscale modeling. *Proc. Symp. Numerical Models of Ocean Circulation*, Nat. Acad. Sci., Washington, DC.

Charney, J., 1973: Planetary fluid dynamics. *Dynamic Meteorology*, P. Morel, Ed., Reidel, 621 pp.

Cheney, R., 1977: Entrapment of SOFAR floats by Gulf Stream rings. *POLYMODE News*, No. 31.

——, and P. Richardson, 1974: Observed decay of a cyconic Gulf Stream ring, Tech. Rep. 74-2, University of Rhode Island, 137 pp.

——, and ——, 1977: Trajectory of a satellite-tracked buoy in a Kuroshio cold ring. *POLYMODE News*, No. 21.

Flierl, G., 1977: The application of linear quasi-geostrophic dynamics to Gulf Stream rings. *J. Phys. Oceanogr.*, **7**, 365–379.

——, 1978: Models of vertical structure and the calibration of two-layer models. *Dyn. Atmos. Ocean.*, **2**, 341–381.

——, and J. McWilliams, 1978: On the stability of barotropic and baroclinic modans. In preparation.

——, V. Larichev, J. McWilliams and G. Reznik, 1979: The dynamics of barotropic and baroclinic solitary eddies. *Dyn. Atmos. Ocean.* (in press).

Fuglister, F., and V. Worthington, 1951: Some results of a multiple ship survey of the Gulf Stream. *Tellus*, **3**, 1–14.

Holland, W., 1978: The role of mesoscale eddies in the general circulation of the ocean—Numerical experiments using a wind-driven quasi-geostrophic model. *J. Phys. Oceanogr.*, **8**, 363–392.

Lai, D., and P. Richardson, 1977: Distribution and movement of Gulf Stream rings. *J. Phys. Oceanogr.*, **7**, 670–683.

Mied, R., 1978: The propagation and energetics of baroclinic eddies on a beta-plane. Unpublished manuscript.

——, and G. J. Lindemann, 1979: The propagation and evolution of cyclonic Gulf Stream rings. *J. Phys. Oceanogr.*, **9**, 1183–1206.

Parker, C., 1971: Gulf Stream rings in the Sargasso Sea. *Deep-Sea Res.*, **18**, 981–993.

Rhines, P., 1977: The dynamics of unsteady currents. *The Sea*, Vol. 6, Interscience, 189–318.

Sandford, T., B. Drever and J. Dunlop, 1978: Mobile deep water velocity profiling in the Local Dynamics Experiment. *POLYMODE News*, No. 44.

Schmitz, J., and A. Vastano, 1975: Entrainment and diffusion in a Gulf Stream cyclonic ring. *J. Phys. Oceanogr.*, **5**, 93–97.

Taft and Baranov *et al.*, 1978: Preliminary interpretation of POLYMODE synoptic XBT data. *POLYMODE News*, No. 47.